Microfabricated High-Speed Axial-Flux Multiwatt Permanent-Magnet Generators—Part I: Modeling

Sauparna Das, *Member, IEEE*, David P. Arnold, *Member, IEEE*, Iulica Zana, *Member, IEEE*, Jin-Woo Park, Mark G. Allen, *Senior Member, IEEE*, and Jeffrey H. Lang, *Fellow, IEEE*

***Abstract*—This paper presents the modeling of permanent-magnet (PM) generators for use in microscale power generation systems. The generators are three-phase, axial-flux, synchronous machines, each consisting of a multipole, surface-wound stator and PM rotor. The machines are modeled by analytically solving two-dimensional (2-D) magneto-quasi-static Maxwell's equations as a function of radius. The 2-D field solutions are then integrated over the radial span of the machine to determine circuit parameters such as open-circuit voltage and inductance as well as hysteresis loss in the stator core and eddy current losses in the stator core and windings. The model provides a computationally fast method to determine power and efficiency of an axial-flux PM machine as a function of geometry, speed, and material properties. The open-circuit voltage predictions are also shown to agree well with 3-D finite-element analysis simulation results. [1700]**

***Index Terms*—AC generators, micromachining, permanent-magnet (PM) machines, power microelectromechanical systems (MEMS).**

I. Introduction

MODERN battery technologies have not kept pace with the rising demand for power by portable electronic devices. This has led to the need for alternative power sources such as microelectromechanical systems (MEMS)-based electric generators that can produce 10–100 W of electrical power. Suitable electric generators could be powered by a variety of prime movers, including liquid flow, pressurized gas, or small combustion engines, such as a microscale gas turbine [1], [2].

MEMS fabrication technologies impose several design constraints for microscale rotating magnetic machines not typically seen at the macroscale. The machines are typically limited to a planar geometry due the constraints of surface/bulk micromachining techniques, whereas their macroscale counterparts often employ a cylindrical geometry. Macroscale permanent-magnet (PM) machines use discrete permanent magnets while microscale machines, such as the ones presented here, may use a multipoled PM annulus. The annulus contains "transition regions" where the rotor magnetization smoothly transitions between north and south poles. The size of these "transition regions" can be of the order of a magnetic pole width, resulting in nonideal magnetization patterns and, thus, reduced voltages induced in the windings. In addition, incorporating hard or soft magnetic materials into the process flow requires subsequent microfabrication steps to occur at low temperature.

The difficulty of using microfabrication to bury windings in slots and closing them over with hats, as is typical in the stators of macroscale magnetic machines, makes surface-wound stators preferable at the microscale. PM machines with slotted stators and therefore small air gaps are also prone to demagnetizing the rotor PM, which is not an issue with surface-wound stators due to their small armature reactance. Furthermore, macroscale machines typically have many turns/pole, ($\sim$ 20-turns/pole). However, due to space limitations, microscale machines will generally have only a few turns/pole ($\sim$ 2–4-turns/pole). Increasing the number of turns/pole would significantly increase the resistance of the stator windings due to minimum feature size constraints.

Microfabrication also limits the thickness of the windings due to constraints on the aspect ratio between winding width and thickness. Winding end turns make up a small percentage of the overall size of macroscale machines. In microscale machines, these end turns can take up considerable area and typically account for a large proportion of the overall winding resistance. The space required for the inner end turns of a planar machine limits the minimum radius of the active area of the machine, while the space required for the outer end turns can double the surface area of the stator.

In contrast to the associated design constraints, MEMS fabrication technologies can improve the performance of microscale magnetic machinery. The ratio of surface area to volume decreases as the length scale is reduced. Heat conduction is proportional to surface area while heat production is proportional to volume. By using microfabrication to make flat rather than round conductors, which are placed in intimate contact

Manuscript received October 15, 2005; revised May 1, 2006. This work was supported in part by the U.S. Army Research Laboratory under the Collaborative Technology Alliance Program (DAAD19-01-2-0010). This work was presented in part at the 18th IEEE International Conference on Micro Electro Mechanical Systems, Miami Beach, FL, January 2005. Subject Editor D.-I. Cho.

S. Das was with the Massachusetts Institute of Technology, Cambridge, MA 02139-4307 USA. He is now with Linear Technology, North Chelmsford, MA 01863 USA (e-mail: sdas@linear.com).

D. P. Arnold was with the Georgia Institute of Technology, Atlanta, GA 30332-0269 USA. He is now with the Department of Electrical and Computer Engineering, University of Florida, Gainesville, FL 32611-6200 USA (e-mail: darnold@ufl.edu).

I. Zana was with the Georgia Institute of Technology, Atlanta, GA 30332-0269 USA. He is now with the Center for Materials for Information Technology, University of Alabama, Tuscaloosa, AL 35487 USA (e-mail: izana@mint.ua.edu).

J.-W. Park was with the Georgia Institute of Technology, Atlanta, GA 30332-0269 USA. He is now with CardioMEMS, Inc., Atlanta, GA 30308 USA (e-mail: jp190@mail.gatech.edu).

M. G. Allen is with the School of Electrical and Computer Engineering, Georgia Institute of Technology, Atlanta, GA 30332-0269 USA (e-mail: mark.allen@ece.gatech.edu).

J. H. Lang is with the Department of Electrical Engineering and Computer Science, Massachusetts Institute of Technology, Cambridge, MA 02139-4307 USA (e-mail: lang@mit.edu).

Digital Object Identifier 10.1109/JMEMS.2006.880282

to the substrate, cooling via the thermal conduction of heat generated by currents in the windings improves. This allows for much higher current densities in the windings than is possible in macroscale machines [3]. Microscale magnetic machines can also match the linear tip speeds of their macroscale counterparts by spinning much faster, near 100 000–1 000 000 rpm. This, combined with the higher current densities allowable in the windings, enables microscale machines with very high power densities.

Given their high rotational speed of 100 000+ rpm, microscale magnetic machines operate at electrical frequencies one to two orders of magnitude higher than typical macroscale machines, typically in the kilohertz to tens of kilohertz range. The high operating electrical frequencies lead to smaller passive filtering components in the power electronic circuits that drive them as motors or generators. The small size of these micromachines also leads to low stator inductances. This allows for both generators and motor drive systems with fast transient responses, but also requires very high switching frequencies (hundreds of kilohertz to low megahertz) in their associated power electronics.

In an electric machine, power conversion occurs through the interaction of the stator currents and rotor flux. In an induction machine, the stator currents create the rotor flux. The maximum flux that can be produced without saturating the rotor or stator back iron is proportional to the volume of the machine. As the machine is scaled down to the micro level, the rotor flux decreases rapidly. The net result is very low electromechanical energy conversion. Previous work from this group focused on the use of magnetic induction machines [3], [4] as potential electric generators. The axial-flux machines were tested as tethered motors to verify their electromechanical performance and demonstrated a peak torque of 2.5 $\mu\mathrm{N}\cdot\mathrm{m}$ [4] but were never tested in generating mode.

PM synchronous machines offer several advantages over induction machines, especially as the size is reduced [5]. First, the PM creates an independent source of rotor flux that is much larger than what can be produced by an induction machine of the same size, leading to much higher power densities. Second, PM machines are more efficient since there are no eddy currents induced in the rotor, assuming conduction and eddy current losses in the stators are equal.

Prior work has been done on planar MEMS PM machines. Several low-speed, axial-flux PM motors have been demonstrated [6]–[8]. PM generators have also been investigated; one has demonstrated an output power of 14.6 mW at 58 000 rpm and high-speed rotation up to 260 000 rpm [9]. Another, a turbine generator powered by gas flow, has produced 1.1 mW at 30 000 rpm [10].

This paper focuses on the modeling of three-phase, surface-wound, axial-flux PM synchronous machines. The machines are modeled analytically so that their performance can be quickly determined as a function of speed, physical dimensions, material properties, and input currents. Since there are no complicated axial structures such as poles and teeth, the surface-wound machines can be modeled as a set of continuum planar layers by solving Maxwell's equations in the magneto-quasi-static (MQS) domain. The magnetic field intensity H and magnetic flux density B in the machine due to the rotor PM and stator currents are solved for as a function of radius and then integrated over the radial span of the machine to determine relevant machine parameters such as open-circuit voltage, inductance, and torque.

This general field theory approach is computationally very fast and has been used to model both cylindrical and linear electric machines [11], [12]. It can be used for a wide range of planar geometries and is especially useful in determining the effects of air gaps that are on the same order of magnitude as the wavelength of the rotor PM or larger. The field solutions are solved in the spatio–temporal frequency domain, which allows for complicated winding patterns and rotor magnetization profiles to be modeled by decomposing them into their respective Fourier components and then solving for fluxes, voltages, currents, etc., for each harmonic component.

To ease the complexity of this analytical approach, ideal properties are often assumed for the ferromagnetic magnetic materials used in the rotor and stator back irons (e.g., linear *B–H* relationship, zero conductivity, and no saturation or hysteresis) or, in some cases, the effects of the back irons are completely ignored by assuming infinite permeabilities. These approximations are not suitable for the design of high-performance microscale machines, because the effects of the back irons cannot be ignored. The machine model must be able to determine how thin the back irons can be without becoming heavily saturated and thus reducing the total flux. It should also be able to determine hysteresis and eddy current losses in the back irons in order to predict machine efficiency as a function of speed, geometry, and material properties. Thus, saturation, hysteresis, and back iron conductivity must all be accurately accounted for.

The model developed in this paper presents methods to accommodate for these effects utilizing the full nonlinear *B–H* relationship. First, an iterative algorithm is used to solve for effective permeabilities for the rotor and stator back irons. Second, the field theory solutions are used to determine hysteresis loss from the back iron's nonlinear *B–H* curve. Finally, eddy current losses in the stator windings due to the fields generated by the rotor permanent magnet are also computed from the field solutions. The use of effective permeabilities in conjunction with the general field theory approach enables the modeling of machines with nonlinear magnetic materials without resorting to time-consuming numerical methods, while maintaining the computational speed of an analytical model and taking advantage of frequency-domain analysis.

This paper also presents ways of computing relevant machine parameters. The Maxwell Stress Tensor is used to find the torque on the rotor by computing the H and B fields at the surface of the rotor and integrating the shear stress over the rotor surface. Use of the Maxwell Stress Tensor allows the calculation of eddy current losses in the stator core without the need to calculate current densities or evaluate volume integrals. The field solutions are also used to compute the inductance and open-circuit voltage of a single phase of the machine. Along with a simple approximation for the winding resistance, an equivalent circuit model for PM machines is given.

To verify the accuracy, the model's open-circuit voltage predictions are compared to 3-D finite-element analysis (FEA) sim-

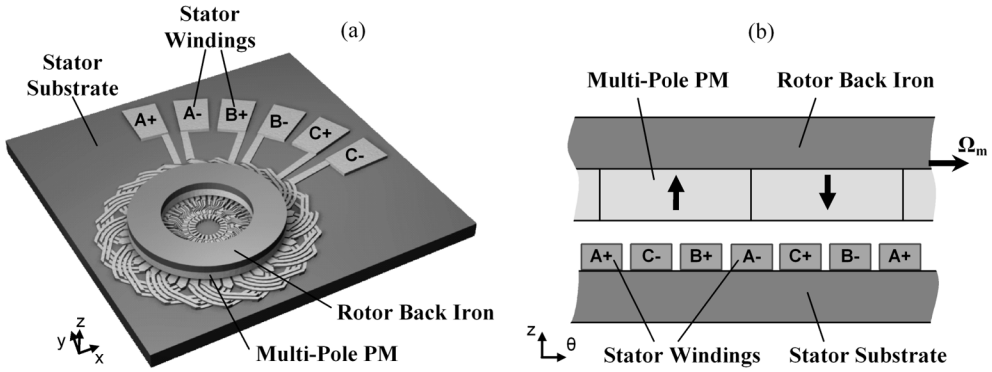

Fig. 1. Conceptual drawing of the PM generator: (a) perspective view and (b) cross section.

ulations. In a companion paper [13], the design, fabrication, and characterization of prototype PM generators are presented, and the experimental results are compared with and match extremely well to the theory.

II. PM Generator Description

The generators are three-phase, eight-pole, axial-flux, synchronous machines [14]. Each machine consists of a rotor with an annular PM and ferromagnetic back iron and a stator with multiturn windings on the surface of a ferromagnetic substrate, which serves as the stator back iron, as shown in Fig. 1.

During operation, the rotating multipoled PM rotor creates a time-varying magnetic flux in the rotor–stator air gap, which induces ac voltages at the terminals of the stator windings. The magnetic flux generated by the PM can be concentrated in the rotor–stator air gap by using back irons with very large permeabilities. By using rare-earth PMs, which have large remanences ($\sim 1\ \mathrm{T}$), strong magnetic fluxes can be generated in the air gap.

In fact, by using high-performance magnetic materials (e.g., PM, rotor and stator back iron) and a suitably thick magnet ($\sim 500\ \mu\mathrm{m}$), the rotor–stator air gap can be made relatively large (300–500 $\mu\mathrm{m}$) to reduce windage loss while maintaining high magnetic flux in the air gap. Thus, the stator windings are designed to occupy space in the air gap on the surface of the stator substrate rather than embedded in slots and closed over with hats, as in the case of previously demonstrated induction machines [3], [4].

This surface-wound scheme offers several design advantages over slotted stators. First, fabrication of windings on the flat stator surface is much simpler. Also, since there are no slots, there is more surface area for the windings, which reduces conduction loss. In addition, cogging, where the poles of the PM tend to align themselves with the gaps between the stator hats, producing torque pulsations and associated loss, is avoided. Finally, when the generator is connected to a load, its ac voltages will produce ac currents through the stator windings. The currents will produce their own magnetic fields (armature reaction) in the air gap. These magnetic fields will have higher order spatial harmonics that interact asynchronously with the rotor PM, producing eddy currents. These rotor eddy currents reduce the overall efficiency, and, in some cases, the heat produced can demagnetize the rotor PM [15]. Due to the large air gap in a surface-wound stator, the magnetic fields produced by the stator currents are very weak, making the eddy current losses in the rotor PM negligible.

III. Modeling

A. Machine Continuum Model

The surface-wound magnetic machine can be modeled as a set of planar continuum layers since there are no complicated axial structures such as poles and teeth, as shown in Fig. 2. The cylindrical geometry (r, θ, z) of the machine is converted to a Cartesian geometry (x, y, z) by unwrapping the machine and setting

$$r \to x, \quad r\theta \to y, \quad z \to z. \tag{1}$$

The rotor–stator air gap, as well as the space above the rotor and below the stator, are modeled as layers with permeability μ_0 and conductivity $\sigma = 0$. The rotor and stator cores (back iron) are modeled as layers with permeabilities μ_r and μ_s and conductivities σ_r and σ_s, respectively. The stator windings are modeled as a layer with zero conductivity and permeability μ_0, with an imposed current density distribution $J_x(y,t)$. The effect of proximity eddy currents within the coil layer is modeled separately in Section I. The rotor *active* layer has a spatially varying magnetization in the axial direction, $M_z(y')$ as well as a permeability μ_a and conductivity σ_a. It can be used to model a PM such as SmCo or NdFeB.

A 2-D Cartesian coordinate convection-diffusion equation for the magnetic vector potential A, derived from Maxwell's equations in the magneto-quasi-static domain, can be solved to find the H and B fields due to the rotor active layer at some radius r [16]. A planar layer moving uniformly with velocity v will have a vector potential with only one component A_x. If no magnetization or independent current sources exist in the layer, then the convection-diffusion equation for A_x is

$$\nabla^2 A_x = \mu\sigma\left(\frac{\partial A_x}{\partial t} + v\frac{\partial A_x}{\partial y}\right). \tag{2}$$

The normal B field and tangential H field can be computed from the vector potential as

$$H_y = \frac{1}{\mu}\frac{\partial A_x}{\partial z} \tag{3}$$

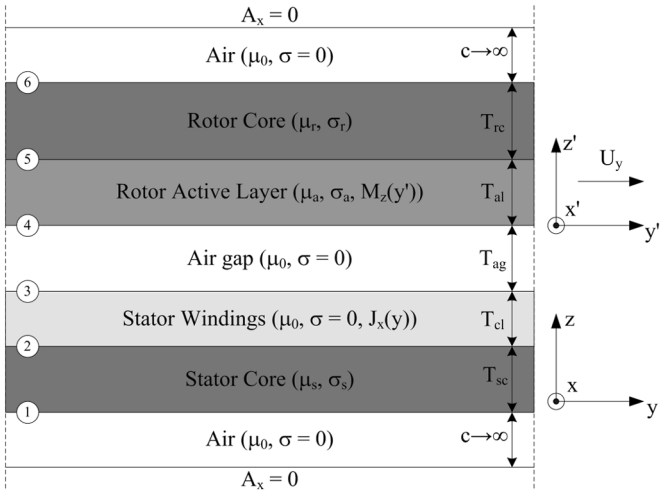

Fig. 2. The PM machine is modeled as a series of planar continuum layers. The rotor moves in the y-direction with velocity U_y. The vector potential A_x is continuous across the interfaces between the layers are designated ①–⑥.

$$B_z = -\frac{\partial A_x}{\partial y}. \tag{4}$$

Equation (2) governs the behavior of the vector potential in the rotor core, stator core, air gap, and regions above the rotor and below the stator, where μ, σ, and v will be different for each layer ($v = U_y$ for the rotor core and zero otherwise). Equation (2) also governs the vector potential in an open-circuited stator winding layer in the PM machine.

In the moving-coordinate frame of the rotor (x', y', z') (Fig. 2), the magnetization profile can be decomposed into its Fourier harmonics

$$M_z(y') = \mathrm{Re}\left\{\sum_{n=-\infty}^{\infty} \hat{M}_{zn} e^{-jnky'}\right\}. \tag{5}$$

The time-varying field in the stationary coordinate frame is found by substituting $y' = y - U_y t$ into (5)

$$M_z(y,t) = \mathrm{Re}\left\{\sum_{n=-\infty}^{\infty} \hat{M}_{zn} e^{jnk(U_y t - y)}\right\}. \tag{6}$$

In addition, U_y can be replaced with the linear velocity at radius r, $U_y = \Omega_m r$, where Ω_m is the angular velocity of the rotor in rad/s. The wavenumber k is simply P/r, where P is the number of pole pairs. Defining $\omega_m \equiv P\Omega_m$, (6) can be rewritten as

$$M_z(y,t) = \mathrm{Re}\left\{\sum_{n=-\infty}^{\infty} \hat{M}_{zn} e^{jn(\omega_m t - ky)}\right\}. \tag{7}$$

In addition, the current density in the stator winding layer J_x will be a function of y and t. The windings on the surface of the stator are arranged so that a traveling magnetic field is created by the winding currents. J_x can be represented in terms of its Fourier harmonics

$$J_x(y,t) = \mathrm{Re}\left\{\sum_{n=-\infty}^{\infty} \hat{J}_{xn} e^{j(\omega_e t - nky)}\right\} \tag{8}$$

where the current in windings is assumed to consist of a single electrical frequency ω_e. Given the forms of the rotor magnetization and stator current density distribution in (7) and (8), respectively, the vector potential in the machine will have the following form:

$$A_x(y,z,t) = \mathrm{Re}\left\{\sum_{n=-\infty}^{\infty} \hat{A}_{xn}(z)\, e^{j(m\omega t - nky)}\right\}. \tag{9}$$

For each spatial harmonic, the complex amplitudes of the normal B field and tangential H field are now

$$\hat{B}_{zn} = jnk\hat{A}_n \tag{10}$$

$$\hat{H}_{yn} = \frac{1}{\mu}\frac{d\hat{A}_n}{dz} \tag{11}$$

where

$$B_z(y,z,t) = \mathrm{Re}\left\{\sum_{n=-\infty}^{\infty} \hat{B}_{zn}(z)\, e^{j(m\omega t - nky)}\right\} \tag{12}$$

$$H_y(y,z,t) = \mathrm{Re}\left\{\sum_{n=-\infty}^{\infty} \hat{H}_{yn}(z)\, e^{j(m\omega t - nky)}\right\}. \tag{13}$$

In (9), (12), and (13), $\omega = \omega_e$ and $m = 1$ for fields generated by stator currents while $\omega = \omega_m$ and $m = n$ for fields generated by the rotor magnetization.

B. Vector Potential Solution in the PM Machine

Using the continuum model developed in Section III-A, the vector potential everywhere in the machine can be found. Each layer in Fig. 2 is the same except for the details of the material properties (μ and σ) and speed. The solution to the convection-diffusion equation (2) for a planar layer with permeability μ, conductivity σ, moving at a constant velocity v and with no magnetization or independent current density will be examined first. By solving for the A, B, and H fields in this planar layer, the field solution for the entire machine can be found by splicing together the solutions of each layer using the appropriate boundary conditions. This approach takes advantage of the fact that A, the normal B field, and tangential H field are all continuous across the interface of two layers. The strategy will be to find the vector potential at interface of the stator core and windings ②, stator windings and air gap ③, air gap and rotor core ④, and the rotor core and permanent magnet ⑤ as functions of the vector potential at the bottom surface of the stator core $A_x^{(1)}$ and at the top surface of the rotor core $\hat{A}_x^{(6)}$. After this has been done, $A_x^{(1)}$ and $\hat{A}_x^{(6)}$ due to the magnetization in the rotor, with the stator currents set to zero, will be found and will be denoted as $A_{x(m)}^{(1)}$ and $\hat{A}_{x(m)}^{(6)}$. Next, $A_x^{(1)}$ and $\hat{A}_x^{(6)}$ due to the stator current distribution, with the rotor magnetization set to zero, will be determined and will be denoted as $A_{x(J)}^{(1)}$ and

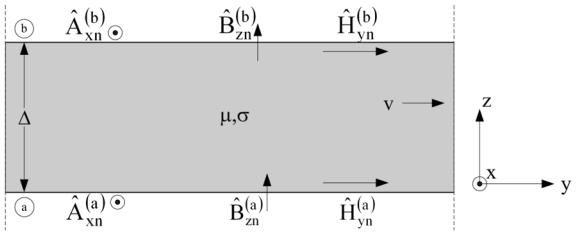

Fig. 3. Lossy magnetic media of thickness Δ moving in the y-direction at a velocity v.

$\hat{A}_{x(J)}^{(6)}$. Using the linear superposition of the two separate solutions, the vector potential and magnetic fields everywhere in the machine can be found. These field solutions are iterated using different values for the permeability of the rotor and stator cores until the correct effective permeabilities are found so that the B fields in the machine lie on the B–H curves of the core materials used.

Substituting (9) into (2), the convection-diffusion equation for the magnetic vector potential yields an ordinary differential equation for each harmonic

$$\frac{d^2\hat{A}_{xn}}{dz^2} = \gamma_n^2 \hat{A}_{xn} \tag{14}$$

in a general layer where

$$\gamma_n = \sqrt{n^2k^2 + j\mu\sigma\,(m\omega - nkv)}. \tag{15}$$

The solution to this equation is presented in terms of the complex vector potential amplitudes at the upper (a) and lower (b) boundaries of the planar layer [17], as shown in Fig. 3. It takes the form

$$\hat{A}_{xn}(z) = \hat{A}_{xn}^{(b)} \frac{\sinh(\gamma_n z)}{\sinh(\gamma_n \Delta)} + \hat{A}_{xn}^{(a)} \frac{\sinh(\gamma_n(\Delta - z))}{\sinh(\gamma_n \Delta)}. \tag{16}$$

To simplify the analysis, transfer relations between the complex amplitudes of H, B, and A at the upper and lower surfaces of each layer are derived [17]. Fig. 3 shows a layer of thickness Δ moving in the y-direction with constant velocity v and having permeability μ and conductivity σ. The vector potential and/or normal B fields at either the top or bottom surface can be computed from the tangential H on both surfaces using

$$\begin{bmatrix} \hat{A}_{xn}^{(b)} \\ \hat{A}_{xn}^{(a)} \end{bmatrix} = \frac{1}{jnk} \begin{bmatrix} \hat{B}_{zn}^{(b)} \\ \hat{B}_{zn}^{(a)} \end{bmatrix} = \frac{\mu}{\gamma_n} \begin{bmatrix} \coth(\gamma_n\Delta) & \frac{-1}{\sinh(\gamma_n\Delta)} \\ \frac{1}{\sinh(\gamma_n\Delta)} & -\coth(\gamma_n\Delta) \end{bmatrix} \begin{bmatrix} \hat{H}_{yn}^{(b)} \\ \hat{H}_{yn}^{(a)} \end{bmatrix}. \tag{17}$$

Conversely, the tangential H on either surface can be computed from the vector potential on both surfaces using

$$\begin{bmatrix} \hat{H}_{yn}^{(b)} \\ \hat{H}_{yn}^{(a)} \end{bmatrix} = \frac{\gamma_n}{\mu} \begin{bmatrix} \coth(\gamma_n\Delta) & \frac{-1}{\sinh(\gamma_n\Delta)} \\ \frac{1}{\sinh(\gamma_n\Delta)} & -\coth(\gamma_n\Delta) \end{bmatrix} \begin{bmatrix} \hat{A}_{xn}^{(b)} \\ \hat{A}_{xn}^{(a)} \end{bmatrix}. \tag{18}$$

The transfer relation matrices (17) and (18) are used to find the vector potential and tangential H at the interfaces of the stator core and windings ②, stator windings and air gap ③, air gap and rotor core ④, and rotor core and PM ⑤, as functions of the vector potential at the bottom surface of the stator core $A_{xn}^{(1)}$ and at the top surface of the rotor core $\hat{A}_{xn}^{(6)}$ (Fig. 2). The following transfer relation constants are defined for the different layers of the machine:

$$\begin{aligned}
\alpha_{1n} &= \frac{\mu_s}{\gamma_{sn}} \frac{\gamma_{0n}}{\mu_0} \sinh(\gamma_{sn}T_{sc}) + \cosh(\gamma_{sn}T_{sc}) \\
\alpha_{2n} &= \frac{\gamma_{sn}}{\mu_s} \sinh(\gamma_{sn}T_{sc}) + \frac{\gamma_{0n}}{\mu_0} \cosh(\gamma_{sn}T_{sc}) \qquad (19a) \\
\alpha_{3n} &= \frac{\mu_0}{\gamma_{0n}} \alpha_{2n} \sinh(\gamma_{0n}T_{\mathrm{cl}}) + \alpha_{1n} \cosh(\gamma_{0n}T_{\mathrm{cl}}) \\
\alpha_{4n} &= \frac{\gamma_{0n}}{\mu_0} \alpha_{1n} \sinh(\gamma_{0n}T_{\mathrm{cl}}) + \alpha_{2n} \cosh(\gamma_{0n}T_{\mathrm{cl}}) \qquad (19b) \\
\alpha_{5n} &= \frac{\mu_0}{\gamma_{0n}} \alpha_{4n} \sinh(\gamma_{0n}T_{\mathrm{ag}}) + \alpha_{3n} \cosh(\gamma_{0n}T_{\mathrm{ag}}) \\
\alpha_{6n} &= \frac{\gamma_{0n}}{\mu_0} \alpha_{3n} \sinh(\gamma_{0n}T_{\mathrm{ag}}) + \alpha_{4n} \cosh(\gamma_{0n}T_{\mathrm{ag}}) \qquad (19c) \\
\alpha_{7n} &= \frac{\mu_a}{\gamma_{an}} \alpha_{6n} \sinh(\gamma_{an}T_{\mathrm{al}}) + \alpha_{5n} \cosh(\gamma_{an}T_{\mathrm{al}}) \\
\alpha_{8n} &= \frac{\gamma_{an}}{\mu_a} \alpha_{5n} \sinh(\gamma_{an}T_{\mathrm{al}}) + \alpha_{6n} \cosh(\gamma_{an}T_{\mathrm{al}}). \qquad (19d)
\end{aligned}$$

Using these constants, the complex amplitudes of the vector potential and tangential H at the interfaces ②, ③, ④, and ⑤ can now be written in terms of $A_{xn}^{(1)}$ as

$$\begin{aligned}
\hat{A}_{xn}^{(2)} &= \alpha_{1n}\hat{A}_{xn}^{(1)} \\
\hat{A}_{xn}^{(3)} &= \alpha_{3n}\hat{A}_{xn}^{(1)} \\
\hat{A}_{xn}^{(4)} &= \alpha_{5n}\hat{A}_{xn}^{(1)} \\
\hat{A}_{xn}^{(5)} &= \alpha_{7n}\hat{A}_{xn}^{(1)} \qquad (20a) \\
\hat{H}_{yn}^{(2)} &= \alpha_{2n}\hat{A}_{xn}^{(1)} \\
\hat{H}_{yn}^{(3)} &= \alpha_{4n}\hat{A}_{xn}^{(1)} \\
\hat{H}_{yn}^{(4)} &= \alpha_{6n}\hat{A}_{xn}^{(1)} \\
\hat{H}_{yn}^{(5)} &= \alpha_{8n}\hat{A}_{xn}^{(1)}. \qquad (20b)
\end{aligned}$$

To find the vector potential and tangential H at the same four interfaces in terms of $A_x^{(6)}$, the following transfer relation constants are defined for the different layers of the machine:

$$\begin{aligned}
\beta_{1n} &= \frac{\mu_r}{\gamma_{rn}} \frac{\gamma_{0n}}{\mu_0} \sinh(\gamma_{rn}T_{rc}) + \cosh(\gamma_{rn}T_{rc}) \\
\beta_{2n} &= \frac{\gamma_n}{\mu_r} \sinh(\gamma_{rn}T_{rc}) + \frac{\gamma_{0n}}{\mu_0} \cosh(\gamma_{rn}T_{rc}) \qquad (21a) \\
\beta_{3n} &= \frac{\mu_a}{\gamma_{an}} \beta_{2n} \sinh(\gamma_{an}T_{\mathrm{al}}) + \beta_{1n} \cosh(\gamma_{an}T_{\mathrm{al}}) \\
\beta_{4n} &= \frac{\gamma_{an}}{\mu_a} \beta_{1n} \sinh(\gamma_{an}T_{\mathrm{al}}) + \beta_{2n} \cosh(\gamma_{an}T_{\mathrm{al}}) \qquad (21b) \\
\beta_{5n} &= \frac{\mu_0}{\gamma_{0n}} \beta_{4n} \sinh(\gamma_{0n}T_{\mathrm{ag}}) + \beta_{3n} \cosh(\gamma_{0n}T_{\mathrm{ag}}) \\
\beta_{6n} &= \frac{\gamma_{0n}}{\mu_0} \beta_{3n} \sinh(\gamma_{0n}T_{\mathrm{ag}}) + \beta_{4n} \cosh(\gamma_{0n}T_{\mathrm{ag}}) \qquad (21c) \\
\beta_{7n} &= \frac{\mu_0}{\gamma_{0n}} \beta_{6n} \sinh(\gamma_{0n}T_{\mathrm{cl}}) + \beta_{5n} \cosh(\gamma_{0n}T_{\mathrm{cl}}) \\
\beta_{8n} &= \frac{\gamma_{0n}}{\mu_0} \beta_{5n} \sinh(\gamma_{0n}T_{\mathrm{cl}}) + \beta_{6n} \cosh(\gamma_{0n}T_{\mathrm{cl}}). \qquad (21d)
\end{aligned}$$

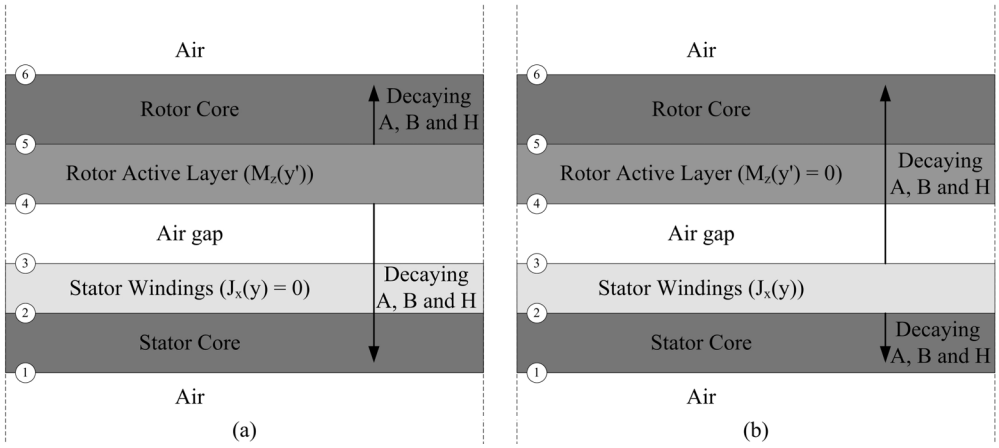

Fig. 4. Spatially decaying fields due to (a) the rotor PM and (b) the stator currents. When solving for the fields due to one source, the other is set to zero.

Using these constants, the complex amplitudes of the vector potential and tangential H at interfaces ②, ③, ④, and ⑤ can now also be written as

$$\begin{aligned}
\hat{A}_{xn}^{(5)} &= \beta_{1n}\hat{A}_{xn}^{(6)} \\
\hat{A}_{xn}^{(4)} &= \beta_{3n}\hat{A}_{xn}^{(6)} \\
\hat{A}_{xn}^{(3)} &= \beta_{5n}\hat{A}_{xn}^{(6)} \\
\hat{A}_{xn}^{(2)} &= \beta_{7n}\hat{A}_{xn}^{(6)} \qquad \text{(22a)} \\
\hat{H}_{yn}^{(5)} &= -\beta_{2n}\hat{A}_{xn}^{(6)} \\
\hat{H}_{yn}^{(4)} &= -\beta_{4n}\hat{A}_{xn}^{(6)} \\
\hat{H}_{yn}^{(3)} &= -\beta_{6n}\hat{A}_{xn}^{(6)} \\
\hat{H}_{yn}^{(2)} &= -\beta_{8n}\hat{A}_{xn}^{(6)}. \qquad \text{(22b)}
\end{aligned}$$

The constants α_{in}, where $|\alpha_{\text{in}}| > 1$, describe the exponential decay in the vector potential and tangential H at interface ① due to some source of magnetic field in the layers above it. The constants β_{in}, where $|\beta_{\text{in}}| > 1$, describe the decay in the vector potential and tangential H at interface ⑥ due to some source of magnetic field in some layer below. The field distributions in the active layer due to the PM and fields in the coil layer due to the stator currents are governed by their own respective vector potential solutions which are given in Sections III-C and -E.

Note that, for a given excitation source (rotor magnetization or stator current), the vector potential at some interface is written in terms of an α or a β parameter and not both. In other words, the two are mutually exclusive. For example, the fields due to the rotor PM will decay spatially as they move further away from the active layer. Referring to Fig. 4(a), the fields will decay below the active layer as they move to the air gap, coil layer, and stator core, and therefore the α parameters are used for interfaces ②–④. Since the fields decay in the rotor core which is above the active layer, the β parameters are used at interface ⑤. The opposite is true for the fields due to the stator currents in the coil layer, as shown in Fig. 4(b). Due to the symmetry of the machine about the air gap layer, the α parameters are used for interface ② while the β parameters are used for interfaces ③–⑤. This summarized in Table I. The values for γ_{0n}, γ_{an}, γ_{rn}, and γ_{sn} are given in Table II. In a synchronous machine, such as a PM machine, the electrical frequency of the stator currents ω_e equals the angular velocity ω_m.

TABLE I
VECTOR POTENTIALS AND TANGENTIAL H AT DIFFERENT INTERFACE LAYERS DUE TO THE ROTOR PM AND STATOR CURRENTS USING α AND β PARAMETERS

Interface	A_x, H_y due to rotor PM	**A_x, H_y due to Stator currents**
①	$\hat{A}^{(1)}_{xn(m)}$, $\frac{\gamma_{0n}}{\mu_0}\hat{A}^{(1)}_{xn(m)}$	$\hat{A}^{(1)}_{xn(J)}$, $\frac{\gamma_{0n}}{\mu_0}\hat{A}^{(1)}_{xn(J)}$
②	$\alpha_{1n}\hat{A}^{(1)}_{xn(m)}$, $\alpha_{2n}\hat{A}^{(1)}_{xn(m)}$	$\alpha_{1n}\hat{A}^{(1)}_{xn(J)}$, $\alpha_{2n}\hat{A}^{(1)}_{xn(J)}$
③	$\alpha_{3n}\hat{A}^{(1)}_{xn(m)}$, $\alpha_{4n}\hat{A}^{(1)}_{xn(m)}$	$\beta_{5n}\hat{A}^{(6)}_{xn(J)}$, $-\beta_{6n}\hat{A}^{(6)}_{xn(J)}$
④	$\alpha_{5n}\hat{A}^{(1)}_{xn(m)}$, $\alpha_{6n}\hat{A}^{(1)}_{xn(m)}$	$\beta_{3n}\hat{A}^{(6)}_{xn(J)}$, $-\beta_{4n}\hat{A}^{(6)}_{xn(J)}$
⑤	$\beta_{1n}\hat{A}^{(6)}_{xn(m)}$, $-\beta_{2n}\hat{A}^{(6)}_{xn(m)}$	$\beta_{1n}\hat{A}^{(6)}_{xn(J)}$, $-\beta_{2n}\hat{A}^{(6)}_{xn(J)}$
⑥	$\hat{A}^{(6)}_{xn(m)}$, $-\frac{\gamma_{0n}}{\mu_0}\hat{A}^{(6)}_{xn(m)}$	$\hat{A}^{(6)}_{xn(J)}$, $-\frac{\gamma_{0n}}{\mu_0}\hat{A}^{(6)}_{xn(J)}$

C. Vector Potentials Due to the Rotor Magnetization Voltage

The vector potential in the machine due to the rotor permanent magnet can now be determined with the aid of the transfer relation constants. For the rotor active layer with magnetization $M_z(y')$ moving uniformly with velocity U_y, the convection-diffusion equation for A_x is

$$\nabla^2 A_x + \mu_a \frac{\partial M_z}{\partial y} = \mu_a \sigma_a \left(\frac{\partial A_x}{\partial t} + U_y \frac{\partial A_x}{\partial y} \right). \qquad (23)$$

Substituting (7) and (9) into (23), the convection-diffusion equation for the magnetic vector potential yields an ordinary differential equation for each harmonic

$$\frac{d^2 \hat{A}_{xn}}{dz^2} = \gamma_{an}^2 \hat{A}_{xn} + j\mu_a nk \hat{M}_{zn}. \qquad (24)$$

The particular solution for a PM annulus is

$$\hat{A}_{xnp} = -j\frac{\mu_a nk}{\gamma_{an}^2}\hat{M}_{zn} = -j\hat{A}_{xn(m)} \qquad (25)$$

TABLE II
DIFFUSION CONSTANTS FOR DIFFERENT PLANAR LAYERS

Diffusion Constant	Value
γ_{0n}	$\sqrt{n^2k^2}$
γ_{an}	$\sqrt{n^2k^2}$
γ_{rn}	$\sqrt{n^2k^2}$
γ_{sn}	$\sqrt{n^2k^2 + j\mu_s\sigma_s n\omega_m}$

since the magnetization only varies with y and not z. The vector potential in the PM layer is

$$\hat{A}_{xn}(z) = \hat{A}_{xn}^{(b)} \frac{\sinh(\gamma_{an} z)}{\sinh(\gamma_{an} T_{\rm al})} + \hat{A}_{xn}^{(a)} \frac{\sinh(\gamma_{an}(T_{\rm al} - z))}{\sinh(\gamma_{an} T_{\rm al})} - j\hat{A}_{xn(m)}. \quad (26)$$

The vector potential at the top of the PM can be written in terms of $\hat{A}_{xn(m)}^{(6)}$, while the vector potential at the bottom can be written in terms of $\hat{A}_{xn(m)}^{(1)}$ (Fig. 5) according to

$$\beta_{1n}\hat{A}_{xn(m)}^{(6)} = \hat{A}_{xn}^{(b)} - j\hat{A}_{xn(m)} \rightarrow \hat{A}_{xn}^{(b)} = \beta_{1n}\hat{A}_{xn(m)}^{(6)} + j\hat{A}_{xn(m)} \quad (27)$$

$$\alpha_{5n}\hat{A}_{xn(m)}^{(1)} = \hat{A}_{xn}^{(a)} - j\hat{A}_{xn(m)} \rightarrow \hat{A}_{xn}^{(a)} = \alpha_{5n}\hat{A}_{xn(m)}^{(1)} + j\hat{A}_{xn(m)}. \quad (28)$$

The subscript (m) has been added to denote that the two vector potentials are due to the PM. Similarly, the tangent H field at the top and bottom surfaces of the PM can be expressed as

$$\hat{H}_{yn}^{(b)} = -\beta_{2n}\hat{A}_{xn(m)}^{(6)} \quad (29)$$

$$\hat{H}_{yn}^{(a)} = \alpha_{6n}\hat{A}_{xn(m)}^{(1)}. \quad (30)$$

Using transfer relation matrices (17) and (18), $\hat{A}_{xn}^{(b)}$ and $\hat{A}_{xn}^{(a)}$ can be eliminated, leaving the following two equations for $A_x^{(1)}$ and $A_x^{(6)}$:

$$\alpha_{6n}\hat{A}_{xn}^{(1)} + \beta_{4n}\hat{A}_{xn}^{(6)} = -j\frac{\gamma_{an}}{\mu_a}\sinh(\gamma_{an}T_{\rm al})\hat{A}_{xn(m)} \quad (31)$$

$$\alpha_{8n}\hat{A}_{xn}^{(1)} + \beta_{2n}\hat{A}_{xn}^{(6)} = -j\frac{\gamma_{an}}{\mu_a}\sinh(\gamma_{an}T_{\rm al})\hat{A}_{xn(m)}. \quad (32)$$

Solving (31) and (32), $\hat{A}_{xn(m)}^{(1)}$ and $\hat{A}_{xn(m)}^{(6)}$ in terms of $\hat{A}_{xn(m)}^{1}$ are

$$\hat{A}_{xn(m)}^{(1)} = -j\frac{\gamma_{an}}{\mu_a}\left[\frac{\beta_{4n} - \beta_{2n}}{\alpha_{8n}\beta_{4n} - \alpha_{6n}\beta_{2n}}\right] \times \sinh(\gamma_{an}T_{\rm al})\hat{A}_{xn(m)} \quad (33)$$

$$\hat{A}_{xn(m)}^{(6)} = -j\frac{\gamma_{an}}{\mu_a}\left[\frac{\alpha_{8n} - \alpha_{6n}}{\alpha_{8n}\beta_{4n} - \alpha_{6n}\beta_{2n}}\right] \times \sinh(\gamma_{an}T_{\rm al})\hat{A}_{xn(m)}. \quad (34)$$

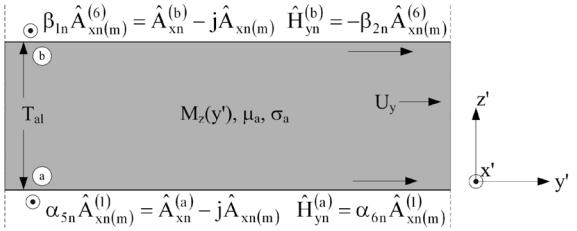

Fig. 5. Boundary conditions for the rotor PM layer.

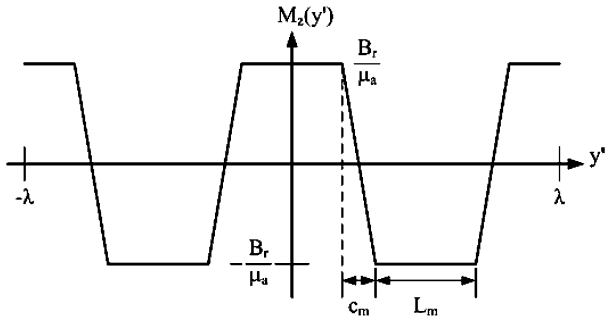

Fig. 6. Trapezoidal magnetization profile of annular PM. B_r is the remanent flux density of the magnet. c_m is the transition region length.

D. Rotor Magnetization Profile

Rotors with an annular PM are used in the generators. For an annular PM, the rotor magnetization, impressed using a magnetic poling process, does not abruptly transition between north and south poles; instead, the magnetic remanence smoothly transitions between $+B_r$ and $-B_r$. Normally, in a macroscale machine, discrete PMs are used so this transition region is not present. However, this effect is important because of the small dimensions of the microscale PM machines. Therefore, the annular rotor PM is modeled with a trapezoidal magnetization profile with a linear "transition region" of length c_m, as shown in Fig. 6. This linear transition is used as a first-order approximation for computational simplicity.

Due to the even symmetry of the profile shown in Fig. 6, the Fourier harmonics of the rotor magnetization in (7) can be expressed as

$$M_z(y,t) = \mathrm{Re}\left\{\sum_{n=1,odd}^{\infty} \hat{M}_{zn} e^{jn(\omega_m t - ky)}\right\} \quad (35)$$

where

$$\hat{M}_{zn} = \frac{1}{\lambda}\int_{\lambda} M_z(y') e^{jnky'} dy. \quad (36)$$

Defining the length of region in which the magnetization is uniform, L_m, to be

$$L_m = \frac{\lambda}{2} - c_m = \frac{\pi r}{P} - c_m \quad (37)$$

the magnitude of each magnetization harmonic is

$$\hat{M}_{zn} = \frac{4}{n^2\pi^2}\frac{\lambda}{c_m}\frac{B_r}{\mu_a}\cos\left(nk\frac{L_m}{2}\right). \tag{38}$$

E. Vector Potentials Due to the Current in the Stator Windings Profile

The vector potential in the machine due to the currents in the stator windings can be determined in the same way they were determined from the rotor permanent magnet. For a planar layer with current density distribution J_x, the governing equation for the vector potential is [17]

$$\nabla^2 A_x = -\mu_0 J_x. \tag{39}$$

Following the same procedure in Section III-C, (8) and (9) are substituted into (39) for the magnetic vector potential, yielding the following ordinary differential equation for each harmonic:

$$\frac{d^2\hat{A}_{xn}}{dz^2} - \gamma_{0n}^2\hat{A}_{nx} = -\mu_0\hat{J}_{xn}. \tag{40}$$

The resulting particular solution to the vector potential for each harmonic in the stator winding layer is

$$\hat{A}_{xn(J)} = \frac{\mu_0}{\gamma_{0n}^2}\hat{J}_{xn}. \tag{41}$$

The vector potential in the stator current layer is

$$\begin{aligned}\hat{A}_{xn}(z) =& \hat{A}_{xn}^{(b)}\frac{\sinh(\gamma_{0n}z)}{\sinh(\gamma_{0n}T_{\rm cl})} \\ &+ \hat{A}_{xn}^{(a)}\frac{\sinh(\gamma_{0n}(T_{\rm cl}-z))}{\sinh(\gamma_{0n}T_{\rm cl})} + \hat{A}_{xn(J)}.\end{aligned} \tag{42}$$

The vector potential at the top of the stator current layer can be written in terms of $\hat{A}_{xn(J)}^{(6)}$ while the vector potential at the bottom can be written in terms of $\hat{A}_{xn(J)}^{(1)}$ according to

$$\begin{aligned}\beta_{5n}\hat{A}_{xn(J)}^{(6)} &= \hat{A}_{xn}^{(b)} + \hat{A}_{xn(J)} \\ &\rightarrow \hat{A}_{xn}^{(b)} = \beta_{5n}\hat{A}_{xn(J)}^{(6)} - \hat{A}_{xn(J)}\end{aligned} \tag{43}$$

$$\begin{aligned}\alpha_{1n}\hat{A}_{xn(J)}^{(1)} &= \hat{A}_{xn}^{(a)} + \hat{A}_{xn(J)} \\ &\rightarrow \hat{A}_{xn}^{(a)} = \alpha_{1n}\hat{A}_{xn(J)}^{(1)} - \hat{A}_{xn(J)}.\end{aligned} \tag{44}$$

The subscript (J) has been added to denote that the two vector potentials are due to the currents in the stator winding. Following the same procedure used for the rotor magnetization, $\hat{A}_{xn(J)}^{(1)}$ and $\hat{A}_{xn(J)}^{(6)}$ in terms of $\hat{A}_{xn(J)}$ are

$$\begin{aligned}\hat{A}_{xn(J)}^{(1)} =& \frac{\gamma_{0n}}{\mu_0}\left[\frac{\beta_{8n}-\beta_{6n}}{\alpha_{4n}\beta_{8n}-\alpha_{2n}\beta_{6n}}\right] \\ &\times \sinh(\gamma_{0n}T_{\rm cl})\,\hat{A}_{xn(J)}\end{aligned} \tag{45}$$

$$\begin{aligned}\hat{A}_{xn(J)}^{(6)} =& \frac{\gamma_{0n}}{\mu_0}\left[\frac{\alpha_{4n}-\alpha_{2n}}{\alpha_{4n}\beta_{8n}-\alpha_{2n}\beta_{6n}}\right] \\ &\times \sinh(\gamma_{0n}T_{\rm cl})\,\hat{A}_{xn(J)}.\end{aligned} \tag{46}$$

F. Stator Current Density Profile

Like the rotor magnetization, the spatially varying current density in the stator windings can be represented in terms of Fourier harmonic components according to

$$J_x(y,t) = \mathrm{Re}\left\{\sum_{n=-\infty}^{\infty}\hat{J}_{xn}e^{j(\omega_e t - nky)}\right\}. \tag{47}$$

For the 1-turn/pole stator winding shown in Fig. 7 and where $\lambda = 2\pi r/P$, the complex magnitude of each spatial harmonic is

$$\begin{aligned}\hat{J}_{xn} =& \frac{6}{n\pi}\sin\left(n\pi\frac{W_{\rm cl}}{\lambda}\right) \\ &\times\Big[(1-(-1)^n)\,J_A(t)\,e^{-j(n\pi/2)} \\ &+ (1-(-1)^n)\,J_B(t)\,e^{j(n\pi/6)} \\ &+ (1-(-1)^n)\,J_C(t)\,e^{j(5n\pi/6)}\Big].\end{aligned} \tag{48}$$

For a balanced three-phase current excitation, the amplitudes of the current density harmonics for the 1-turn/pole machine simplify to

$$\begin{aligned}\hat{J}_{xn} = \frac{6}{n\pi}\sin\left(n\pi\frac{W_{\rm cl}}{\lambda}\right)e^{-j(n\pi/2)}J_o, \\ \text{for } n = 1,-5,7,-11,13\ldots.\end{aligned} \tag{49}$$

The current density in a single radial conductor for a machine with a single winding layer is

$$J_o = \frac{I_o}{W_{\rm cl}T_{\rm cl}} \tag{50}$$

where $W_{\rm cl}$ and $T_{\rm cl}$ are the width and thickness of the stator winding, respectively. Note that $W_{\rm cl}$ can be a function of radius so that windings with variable widths can be modeled.

Machines with more than 1-turn/pole can also be modeled using this approach, where the multiple turns can all reside on a single layer or be stacked onto multiple layers. Referring to Fig. 8, harmonic amplitudes for the current density of a single layer 2-turn/pole machine are

$$\begin{aligned}\hat{J}_{xn} = \frac{6}{n\pi}\sin\left(n\pi\frac{W_{\rm cl}}{\lambda}\right)\left(e^{-j(n5\pi/12)} + e^{-j(n7\pi/12)}\right)J_o, \\ \text{for } n = 1,-5,7,-11,13\ldots.\end{aligned} \tag{51}$$

For a machine with a double-layer winding as depicted in Fig. 9, the coils are treated as a single conductor and $T_{\rm cl}$ in this case is the sum of the thicknesses of the top coil, bottom coil, and via layers. The harmonic amplitudes for this winding pattern is also given by (51), where the current density is

$$J_o = \frac{2I_o}{W_{\rm cl}T_{\rm cl}}. \tag{52}$$

In general, for a three-phase surface-wound machine with P pole pairs, N-turns/pole, and κ winding layers, the harmonic

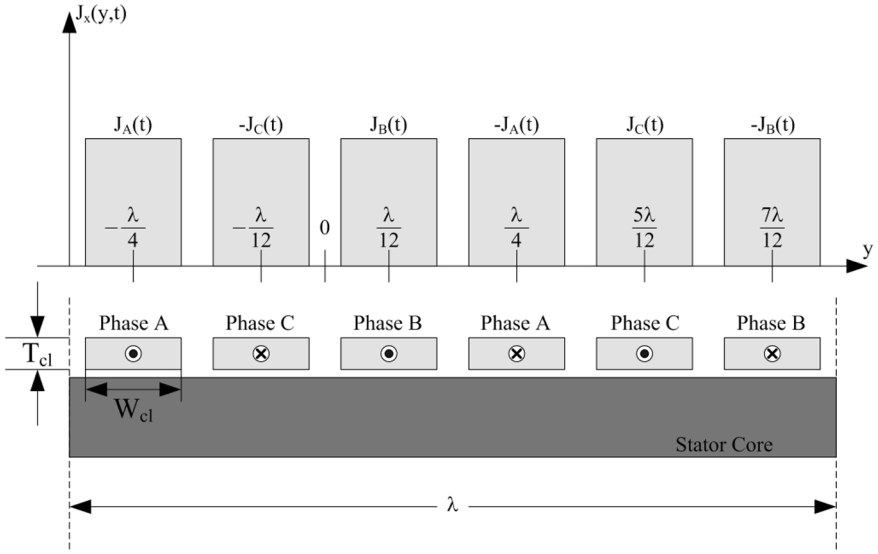

Fig. 7. Current density distribution for a 1-turn/pole surface-wound stator.

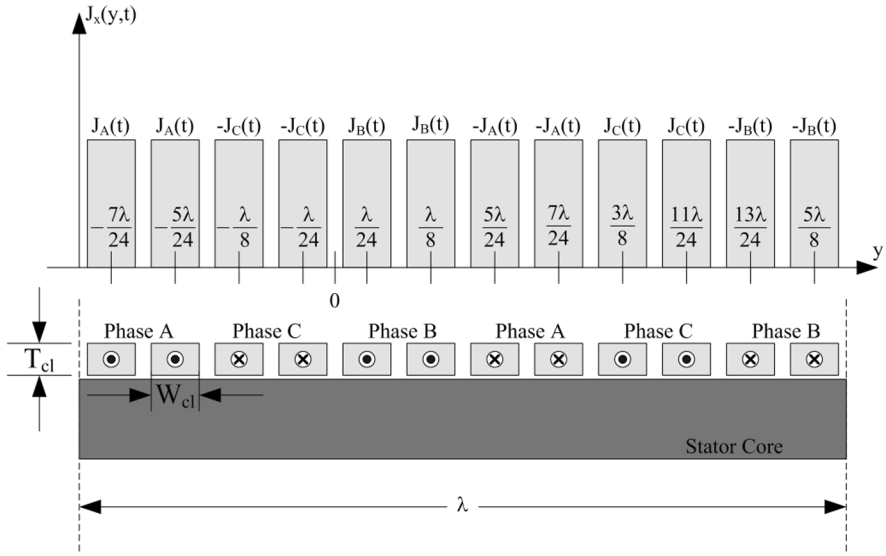

Fig. 8. Current density distribution for a 2-turn/pole surface-wound stator.

amplitudes of the current density are

$$\hat{J}_{xn} = \frac{6}{n\pi}\sin\left(n\pi\frac{W_{\rm cl}}{\lambda}\right) J_o \sum_{\substack{\nu=2N'+1 \\ \text{step } 2}}^{4N'-1} e^{-j(n\pi/6N')\nu},$$
$$\text{for } n = 1, -5, 7, -11, 13\ldots \tag{53}$$

and

$$J_o = \frac{\kappa I_o}{W_{\rm cl} T_{\rm cl}} \tag{54}$$

where $N' = N/\kappa$ and $T_{\rm cl}$ is the total height of all κ winding layers. For current density amplitudes given by (53), the resulting particular solution to (40) is

$$\hat{A}_{xn(J)} = \frac{6}{n\pi}\frac{\mu_0 J_o}{n^2 k^2}\sin\left(n\pi\frac{W_{\rm cl}}{\lambda}\right) \sum_{\substack{\nu=2N'+1 \\ \text{step } 2}}^{4N'-1} e^{-j(n\pi/6N')\nu}. \tag{55}$$

G. Eddy Current Losses in the Stator Core

The eddy current losses in the stator core can be found by computing the drag torque on the rotor generated by these currents. The Maxwell Stress Tensor [18] is used to find the torque on the rotor using the field solutions found for the air gap in the continuum model. Fig. 10 shows the surface over which the stress tensor is computed. The time-averaged force on surfaces 1 and 3 cancel each other. Surface 4 is assumed to be far away from the surface of the rotor core so that the fields there are zero. Therefore, only surface 2 contributes to the time-averaged torque. The time-averaged shear stress at surface 2 is

$$\langle \tau_{yz} \rangle = \frac{1}{2}\sum_n \mathrm{Re}\left\{\hat{B}_{zn}^{(4)}\hat{H}_{yn}^{(4)^*}\right\}. \tag{56}$$

The normal B field and tangential H field at the bottom surface

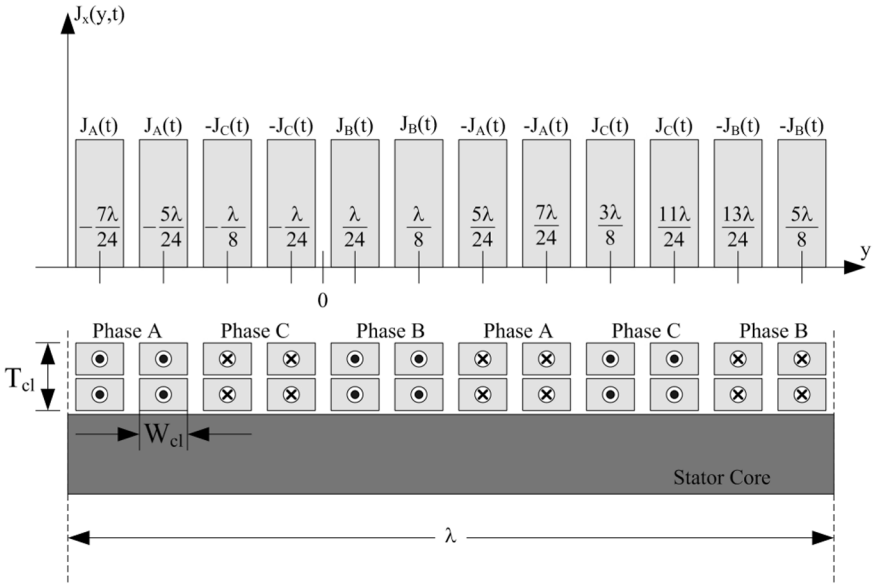

Fig. 9. Current density distribution for a 4-turn/pole double-layer winding.

of the rotor PM are

$$\hat{B}_{zn}^{(4)} = jnk\alpha_{5n}\hat{A}_{xn(m)}^{(1)} \tag{57}$$

$$\hat{H}_{yn}^{(4)} = \alpha_{6n}\hat{A}_{xn(m)}^{(1)}. \tag{58}$$

Substituting (57) and (58) into (56) gives the shear stress on the rotor due to eddy currents in the stator induced by the spinning PM. They are

$$\langle \tau_{yz} \rangle = \sum_n \mathrm{Re}\left\{ jnk\alpha_{5n}\alpha_{6n}^{*} \right\} \left| \hat{A}_{xn(m)}^{(1)} \right|^2. \tag{59}$$

Note that the time-averaged stress is independent of $y = r\theta$ so that the total drag is just 2π times the integral of the r times the shear stress integrated over the radial span of the machine

$$T_{\mathrm{drag}} = -2\pi \int_{r=R_i}^{r=R_o} \langle \tau_{yz} \rangle \, r^2 dr. \tag{60}$$

The minus sign in front of the integral is due to the fact that integration is over surface 2, which has a normal in the $-\hat{z}$ direction. Physically, this drag torque manifests as eddy current loss and stator core heating and can be minimized by using a ferrite or laminated core.

H. Saturation and Hysteresis Loss

Saturation effects in the machine are incorporated into the model by assigning effective permeabilities to the rotor and stator so that the magnitudes of the*B* field in those parts lie on the core material's *B–H* curve. The permeability is found iteratively, as shown in Fig. 11. The procedure starts with some initial value of the permeability in the rotor and stator core $\mu_{i,1}$, where the i stands for (r)otor or (s)tator. Using these values, the magnitudes of the B fields throughout the various parts of the machine are determined using the continuum model (① in Fig. 11). Once the magnitudes of the *B* fields are computed, the corresponding *H* fields are found using the current permeability (② in Fig. 11),

$$H_{i,1} = \frac{B_{i,1}}{\mu_{i,1}}, \qquad \text{for } i = r, s. \tag{61}$$

Since $\mu_{i,1}H_{i,1}$ does not lie on the core material's *B–H* curve, a new permeability is then computed for each section of the machine (③ in Fig. 11) as follows:

$$\mu_{i,2} = \frac{B\left(H_{i,1}\right)}{H_{i,1}}. \tag{62}$$

The new permeability $\mu_{i,2}$ is sent back to the machine model, and the B field is recalculated in every section of the machine (④ in Fig. 11). This process is repeated to find a new H field $H_{i,2}$ and a new permeability $\mu_{i,3}$. Solving for the B fields, it is found that, using $\mu_{i,3}$, these values lie on the *B–H* curve (⑤ and ⑥ in Fig. 11). Therefore, $\mu_{i,3} = \mu_{i,\mathrm{final}}$ will be used in the machine model to compute torque and voltages in the machine. This example has only three iterations but in practice can take up to 20.

Since the B fields in the rotor and stator cores vary spatially over one wavelength, a number of different quantities can be sent to the permeability algorithm. The three quantities chosen are the mean, rms, and peak magnitudes of the B field

$$B_i = \frac{1}{2\pi}\int_0^{2\pi} B_m^{(j)}(\theta) d\theta \tag{63}$$

$$B_i = \sqrt{\frac{1}{2\pi}\int_0^{2\pi} \left[B_m^{(j)}(\theta)\right]^2 d\theta} \tag{64}$$

$$B_i = \max_\theta \left(B_m^{(j)}(\theta) \right). \tag{65}$$

In (63)–(65), $\theta = \omega_m t - nky$ and $B_m^{(j)}$ is the magnitude of the B field at some interface and is given by (66), shown at the

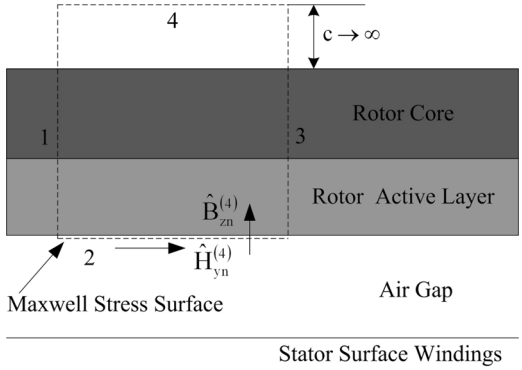

Fig. 10. Maxwell stress surface for torque calculations.

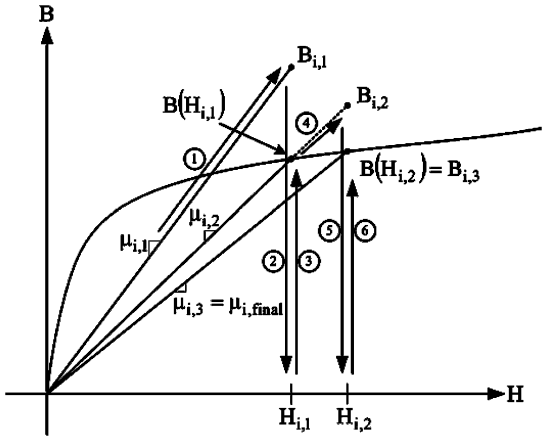

Fig. 11. Nonlinear B-H curve and linearized approximations to the material permeability.

bottom of the page. $B_m^{(j)}$ in the rotor and stator are computed at the bottom surface of the rotor core ($j = 5$) and top surface of stator core ($j = 2$), respectively, both at the middle radius. The predicted open-circuit voltage obtained by using the three different quantities will be compared to FEA simulations to determine which one produces the most accurate result.

The hysteresis loss in the stator core is calculated using the *B–H* curve of the core material. The *B–H* curve for the Moly Permalloy, measured using a vibrating sample magnetometer (VSM), is shown in Fig. 12. The core loss density is defined to be the energy dissipated traversing the *B–H* loop. For material with a peak flux density B_1, the core loss density is [19]

$$\rho_{\text{core}}(B_1) = \int_{-B_1}^{B_1} H(B)\, dB. \tag{67}$$

The peak flux density at some depth in the stator core can be found by reconstructing B_m as a function of z over one period

$$B_1(z) = \max_\theta \left(\sqrt{B_y^2(z,\theta) + B_z^2(z,\theta)} \right) \tag{68}$$

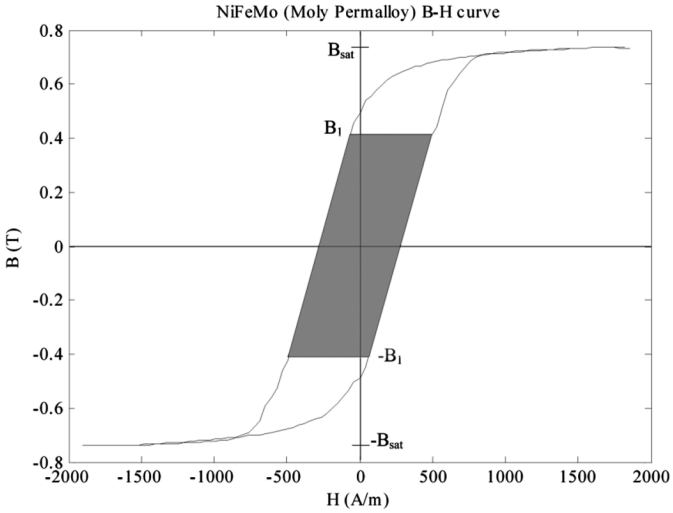

Fig. 12. *B–H* loop for Moly Permalloy. The shaded region is the energy dissipated in a cycle for a peak B field of B_1.

where

$$B_y(z,\theta) = \text{Re}\left\{ \mu_s \sum_{n=1,\text{odd}}^{\infty} \left(\frac{\gamma_n}{\mu_0} \frac{\sinh(\gamma_{sn}(T_{sc} - z))}{\sinh(\gamma_{sn} T_{sc})} + \alpha_{2n} \frac{\sinh(\gamma_{sn} z)}{\sinh(\gamma_{sn} T_{sc})} \right) \hat{A}_{xn(m)}^{(1)} e^{jn\theta} \right\} \tag{69}$$

$$B_z(z,\theta) = \text{Re}\left\{ \sum_{n=1,\text{odd}}^{\infty} jnk \left(\frac{\sinh(\gamma_{sn}(T_{sc} - z))}{\sinh(\gamma_{sn} T_{sc})} + \alpha_{1n} \frac{\sinh(\gamma_{sn} z)}{\sinh(\gamma_{sn} T_{sc})} \right) \hat{A}_{xn(m)}^{(1)} e^{jn\theta} \right\}. \tag{70}$$

The total core loss is the sum of the total energy dissipated in the stator core times the frequency at which the *B–H* loop is traversed

$$\begin{aligned} P_{\text{core}} &= \frac{\omega_m}{2\pi} \int\int\int \rho_{\text{core}}(B_1)\, dV \\ &= \frac{\omega_m}{2} \left(R_o^2 - R_i^2 \right) \int_0^{T_{sc}} \rho_{\text{core}}(B_1(z))\, dz. \end{aligned} \tag{71}$$

I. Proximity Eddy Current Loss in the Stator Windings

The continuum model of the surface wound machine does not model the stator windings as a layer with conductivity σ_c because it is made up of discrete conductors. There are $6N$ radial conductors per wavelength of the rotor magnetization, and

$$B_m^{(j)}(\theta) = \sqrt{\left[\text{Re}\left\{ \sum_{n=1,odd}^{\infty} \hat{B}_{yn}^{(j)} e^{jn\theta} \right\} \right]^2 + \left[\text{Re}\left\{ \sum_{n=1,odd}^{\infty} \hat{B}_{zn}^{(j)} e^{jn\theta} \right\} \right]^2}. \tag{66}$$

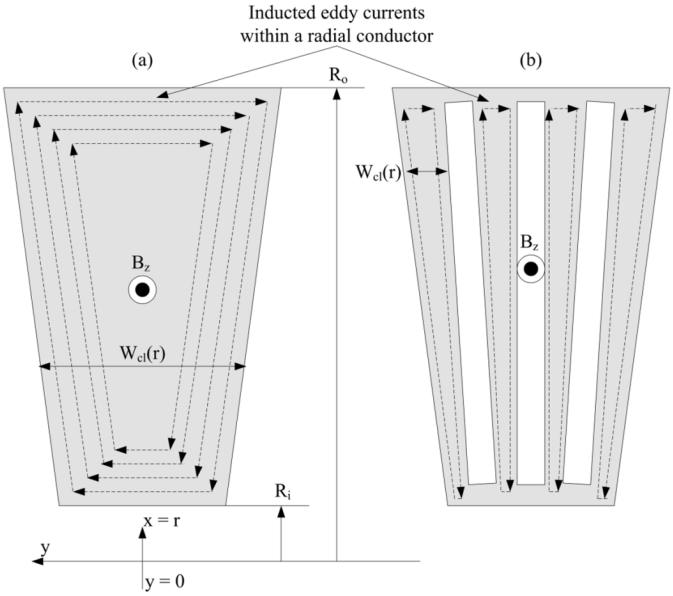

Fig. 13. Proximity eddy currents in radial conductors: (a) unlaminated and (b) laminated.

the width of each of these conductors is much smaller than that wavelength. Instead, the coil layer is treated as a layer with zero conductivity and impose current density $J_x(y,t)$ in the continuum model. The fields in the machine, due to the stator currents, are computed by solving for the vector potential due to this current distribution.

However, eddy currents within each radial conductor will be present as shown in Fig. 13(a). These eddy currents are driven by the magnetic fields from the rotor PM, and the resulting losses are modeled separately using the field solutions from the continuum model as inputs. The B field from the rotor magnetization is used to compute the induced electric field using Faraday's Law. The power dissipation in the radial conductor can then be calculated by integrating the conduction loss density over the volume of the radial conductor. If the losses due these eddy currents are too large, they can be reduced by laminating the radial conductors as shown in Fig. 13(b). The eddy currents in the conductors will produce their own magnetic fields which retard the flux generated by the rotor magnetization. Ampere's Law is used to compute this retarding B field. So long as this B field is much smaller than the B field due to the rotor PM, than the assumption that the conductivity of the coil layer can be ignored in the continuum model will remain valid.

The induced electric field within a radial conductor can be found using Faraday's Law

$$\oint \bar{E} \cdot d\bar{l} = -\frac{\partial}{\partial t} \int \bar{B} \cdot d\bar{A}. \tag{72}$$

The contour for the electric field is assumed to be rectangular and is mainly in the x direction, as shown in Fig. 13. The path lengths in the y-direction at the inner and outer radii are assumed to be small with respect to the radial path and are ignored in this analysis. Therefore, (72), for each harmonic component of the induce electric field, becomes

$$2x\hat{E}_{xn} = -jn\omega_m \hat{B}_{zn,\mathrm{coil}(m)} xy \tag{73}$$

where $\hat{B}_{zn,\mathrm{coil}(m)}$ is

$$\hat{B}_{xn,\mathrm{coil}(m)} = jnk\hat{A}^{(1)}_{xn(m)} \left(\alpha_{1n} + \alpha_{3n}\right) \frac{\sinh\left(0.5\gamma_{0n}T_{\mathrm{cl}}\right)}{\sinh\left(\gamma_{0n}T_{\mathrm{cl}}\right)}. \tag{74}$$

The induced electric field is

$$\hat{E}_{xn} = -0.5jn\omega_m \hat{B}_{zn,\mathrm{coil}(m)} y. \tag{75}$$

The time-averaged power loss density in the radial conductor is

$$\left\langle \sigma_c E^2_{xn}(t) \right\rangle_t = \frac{\sigma_c}{2} \left|\hat{E}_{xn}\right|^2 = \frac{\sigma_c}{4} \left(n\omega_m\right)^2 \left|\hat{B}_{zn,\mathrm{coil}(m)}\right|^2 y^2. \tag{76}$$

The loss density increases with the square of the distance from the center of the radial conductor. The power dissipated in the radial conductor for each harmonic component of the B field due to the rotor PM is

$$P_{\mathrm{radn}} = 2T_{\mathrm{cl}} \int_{R_i}^{R_o} \left(\int_0^{(W_{\mathrm{cl}}(r)/2)} \frac{\sigma_c}{4} \left(n\omega_m\right)^2 \times \left|\hat{B}_{zn,\mathrm{coil}(m)}\right|^2 y^2 dy \right) dr. \tag{77}$$

Evaluating (77) gives

$$P_{\mathrm{radn}} = \frac{\sigma_c}{96} \left(n\omega_m\right)^2 \left|\hat{B}_{zn,\mathrm{coil}(m)}\right|^2 \left(\frac{3PNC_{\mathrm{lam}}}{4\pi}\right) T_{\mathrm{cl}} \left(W_{\mathrm{cl}}\left(R_o\right)^4 - W_{\mathrm{cl}}\left(R_i\right)^4\right). \tag{78}$$

There are $6PN$ radial conductors in a surface-wound stator. If each of these conductors has C_{lam} laminations, then the total loss due to proximity eddy currents is

$$P_{\mathrm{prox}} = \frac{3\sigma_c\omega_m^2}{64\pi} \left(PNC_{\mathrm{lam}}\right)^2 T_{\mathrm{cl}} \times \left[W_{\mathrm{cl}}\left(R_o\right)^4 - W_{\mathrm{cl}}\left(R_i\right)^4\right] \sum_{n=1,\mathrm{odd}}^{\infty} n^2 \left|\hat{B}_{zn,\mathrm{coil}(m)}\right|^2. \tag{79}$$

To better understand how this power dissipation scales, assume that width of the radial conductors is taken to be at $r = (1/2)(R_o - R_i) = R_m$ and is constant over the radial span of the conductor and that g_{cl} is zero. Substituting $P\Omega_m$ for ω_m and revaluating (77), the proximity loss will be

$$P_{\mathrm{prox}} = \left(6NC_{\mathrm{lam}}\right) \frac{\sigma_c}{96} T_{\mathrm{cl}} \left(R_o - R_i\right) \left(\frac{\pi R_m}{3NC_{\mathrm{lam}}}\right)^3 \times \sum_{n=1,\mathrm{odd}}^{\infty} \left(n\Omega_m\right)^2 \left|\hat{B}_{zn,\mathrm{coil}(m)}\right|^2. \tag{80}$$

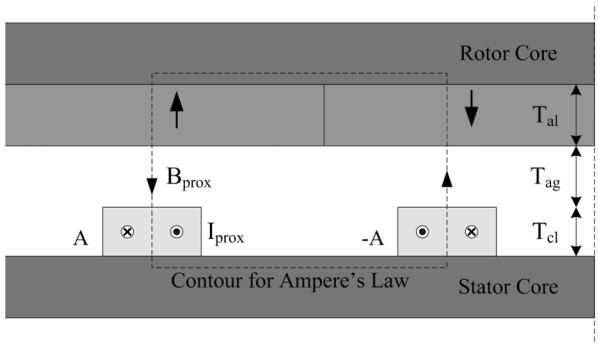

Fig. 14. Proximity eddy current distribution in a single phase and contour for computing the B field due to these currents.

The proximity effect loss increases with the square of the speed and flux density. However, they scale as the inverse square of the number of turns/pole and number of coil laminations. Increasing N and $C_{\rm lam}$ increases the number of radial conductors but reduces the width of each radial conductor. The power dissipated in each conductor is reduced faster than the increase in the number of total radial conductors because its dissipation scales as the cube of the width while the number of conductors is only linear with N and $C_{\rm lam}$. Notice, however, that the proximity loss is independent of the number of pole pairs, P.

In order for the zero conductivity assumption for the coil layer used in the continuum model to be valid, the B field generated by these proximity eddy currents should be much smaller than the B fields due to the rotor PM. To find this proximity effect on the B field, the current through half a radial conductor is computed due the fundamental harmonic of the rotor PM flux. This current is at a maximum at the outer radius where the conductor is widest. Integrating the electric field over half the width of a radial conductor the proximity effect current is

$$\begin{aligned}\hat{I}_{\rm prox} &= \sigma_c T_{\rm cl} \int_0^{(W_{\rm cl}(R_o)/2)} \hat{E}_{x1} dy \\ &= -j\frac{\sigma_c \omega_m}{16} T_{\rm cl} W_{\rm cl}(R_o)^2 \hat{B}_{z1,{\rm coil}(m)}. \end{aligned} \tag{81}$$

Fig. 14 shows how the proximity effect currents are distributed in the windings of phase A. The return path of phase A, denoted as $-A$, has the opposite proximity current distribution. The peak proximity effect B field can be computed, via Ampere's Law, using the contour in Fig. 14 and is given by

$$\hat{B}_{\rm prox} = \frac{\mu_0 \hat{I}_{\rm prox}}{(T_{\rm al} + T_{\rm ag} + T_{\rm cl})}. \tag{82}$$

The ratio of the proximity B fields to the fundamental of the rotor PM B field is equal to

$$\left| \frac{\hat{B}_{\rm prox}}{\hat{B}_{z1,{\rm coil}(m)}} \right| = \frac{\mu_0 \sigma_c \omega_m T_{\rm cl} W_{\rm cl}(R_o)^2}{16(T_{\rm al} + T_{\rm ag} + T_{\rm cl})} \ll 1. \tag{83}$$

Equation (83) should be no more than 0.05 in order for the continuum model to be valid.

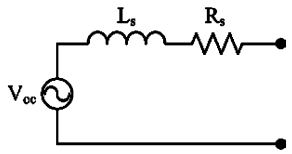

Fig. 15. Equivalent circuit for a single phase of a PM machine consisting of an open-circuit voltage $V_{\rm oc}$, stator winding inductance L_s, and resistance R_s.

IV. Equivalent Circuit Model

To design the complete electric power system, it is useful to have a circuit model of the generator. The equivalent circuit for a single phase of the balanced PM machine is show in Fig. 15. It consists of a back EMF source or open-circuit voltage $V_{\rm oc}$ due the spinning PM as well as an inductance L_s and resistance R_s due to the stator windings. The open-circuit voltage and stator inductance can be found using the vector potential solutions to the machine due the rotor magnetization and stator currents, respectively. The resistance is calculated based on the dimensions of radial conductors and the inner/outer end turns of the stator windings.

A. Open-Circuit Voltage

The spinning multipole PM rotor creates a time-varying flux that induces a voltage $V_{\rm oc}$ on each phase of the stator windings governed by Faraday's Law

$$V_{\rm oc} = \frac{d\lambda_m}{dt} \tag{84}$$

where λ_m is the total flux from the rotor PM linked by a single phase. In order to determine the open-circuit voltage, the axial flux through a single phase of the stator windings must be found. This is achieved by integrating the incremental flux at a given radius over the radial span of the machine. The incremental flux from a single turn can be found by taking the difference between the vector potential [17] of the two radial conductors in that turn (Fig. 16). For instance, if the radial conductors of phase A of a 1-turn/pole machine spans from $y = y_1$ to $y = y_2$, then the incremental flux in that loop is

$$\begin{aligned}\hat{\Phi}_{zn,{\rm coil}(m)} &= \int_{y_1}^{y_2} \hat{B}_{zn,{\rm coil}(m)} e^{-jnky} dy \\ &= \hat{A}_{xn,{\rm coil}(m)} \left(e^{-jnky_1} - e^{-jnky_2} \right) \end{aligned} \tag{85}$$

where $\hat{A}_{xn,{\rm coil}(m)}$ is the vector potential evaluated at half the axial thickness of the stator winding layer

$$\hat{A}_{xn,{\rm coil}(m)} = \hat{A}^{(1)}_{xn(m)} (\alpha_{1n} + \alpha_{3n}) \frac{\sinh(0.5\gamma_{0n} T_{\rm cl})}{\sinh(\gamma_{0n} T_{\rm cl})}. \tag{86}$$

The incremental flux linked by a single phase is P times the flux/pole. From Fig. 16, the incremental flux/phase in phase A of a 1-turn/pole machine is

$$\begin{aligned}\hat{\Phi}_{zn,{\rm coil}(m)} &= P\hat{A}_{xn,{\rm coil}(m)} \left(e^{-jnk(-(\lambda/4))} - e^{-jnk(\lambda/4)} \right) \\ &= 2P\hat{A}_{xn,{\rm coil}(m)} e^{j(n\pi/2)}. \end{aligned} \tag{87}$$

Machines with more than 1-turn/pole can also be modeled using this approach, where the contributions of each turn are

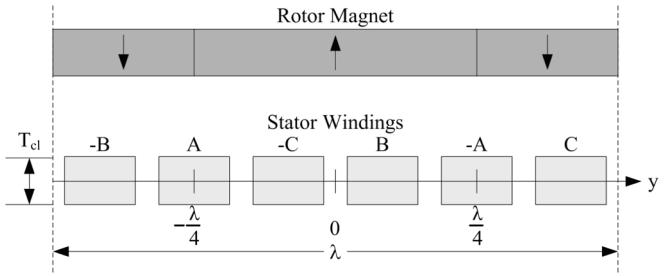

Fig. 16. Voltage calculation diagram for a 1-turn/pole machine. Flux linked by phase A is equal to the difference in the vector potential between $y = 1/4\lambda$ and $y = -1/4\lambda$ evaluated at half the thickness of the stator coils.

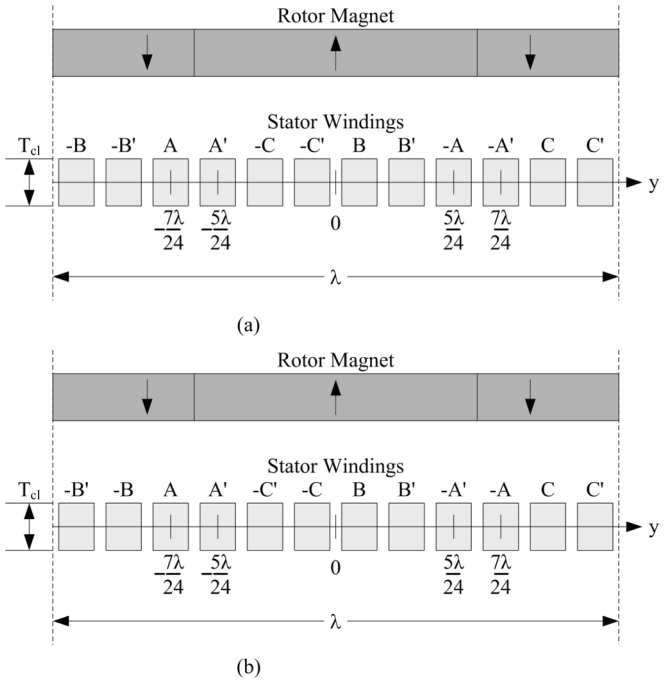

Fig. 17. Voltage calculation diagram for 2-turn/pole machines with (a) full-pitched windings and (b) concentric windings. A and $-A$ constitute a single turn while A' and $-A'$ constitute the second turn.

summed to find the incremental flux/pole. The multiple turns can all reside on a single layer or be stacked onto multiple layers [13]. A cross section of a 2-turn/pole machine is shown in Fig. 17 for both full-pitched and concentric windings. A full-pitched winding is one that spans 180 electrical degrees or a half wavelength [14]. Multiturn concentric windings are made up of long-pitched and short-pitched windings such as A, $-A$ (long) and A', $-A'$ (short) in Fig. 17. The conductors are in the same location for full-pitched and concentric windings and, since the flux through the windings is the net difference in vector potentials, the incremental flux/phase is the same. Referring to Fig. 17 for a 2-turn/pole machine with either full-pitched or concentric windings, the incremental flux/phase is

$$\begin{aligned}\hat{\Phi}_{zn,\text{coil}(m)} &= P\hat{A}_{xn,\text{coil}(m)} \\ &\quad\times\Big(e^{-jnk(-(7\lambda/24))} - e^{-jnk(5\lambda/24)} \\ &\qquad + e^{-jnk(-(5\lambda/24))} - e^{-jnk(7\lambda/24)}\Big) \\ &= 2P\hat{A}_{xn,\text{coil}(m)}\left(e^{jn(7\pi/12)} + e^{jn(5\pi/12)}\right).\end{aligned} \tag{88}$$

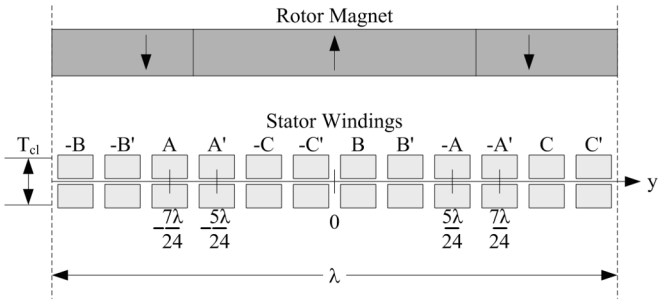

Fig. 18. Voltage calculation diagram a 4-turn/pole machine with double-layer windings. For a machine with a double-layer winding, T_{sw} is the sum of the thicknesses of the top and bottom coils.

This cross section can also be used to model a 4-turn/pole machine that uses two layers of coils with each layer having the same phase sequence as the 2-turn/pole machine $(AA' - C - C' \ldots)$ as shown in Fig. 18. In the case of the 4-turn/pole double-winding-layer machine, the thickness of the stator winding layer T_{cl} is the sum of the thicknesses of the top and bottom coils. For a 4-turn/pole machine using two winding layers, the incremental flux/phase is

$$\hat{\Phi}_{zn,\text{coil}(m)} = 4P\hat{A}_{xn,\text{coil}(m)}\left(e^{jn(7\pi/12)} + e^{jn(5\pi/12)}\right). \tag{89}$$

In general, for a three-phase surface-wound machine with P pole pairs, N-turns/pole, κ winding layers, and $N' = N/\kappa$, the incremental flux/phase is

$$\hat{\Phi}_{zn,\text{coil}(m)} = 2\kappa P\hat{A}_{xn,\text{coil}(m)} \sum_{\substack{\nu=2N'+1 \\ \text{step } 2}}^{4N'-1} e^{(jn\pi/6N'\nu)}. \tag{90}$$

Integrating over the radial span of the machine, the total flux linked by a single phase for each harmonic is

$$\hat{\lambda}_{n,\text{coil}(m)} = \int_{r=R_i}^{r=R_o} \hat{\Phi}_{zn,\text{coil}(m)}dr. \tag{91}$$

The harmonic amplitudes of the open-circuit voltage induced by this flux is

$$\hat{V}_{\text{ocn}} = \frac{d}{dt}\hat{\lambda}_{n,\text{coil}(m)} = jn\omega_m\hat{\lambda}_{n,\text{coil}(m)}. \tag{92}$$

To derive some insight into how various parameters affect the open-circuit voltage, the continuum model can be simplified. To do so, let the magnetization profile approach an ideal square wave ($c_m \to 0$). Also, assume that the rotor and stator cores and rotor active layer (PM) are ideal: μ_r and $\mu_s \to \infty$ and σ_r, σ_s, and $\sigma_a = 0$. In addition, assume that the wavelength is much larger than the thicknesses of the air gap, stator windings, rotor PM and rotor and stator cores: $\gamma_n T_i \ll 1$ (for $i =$ sc, rc, al, cl, and ag). This last approximation means that the exponential decay of the fields in the machine can be ignored. In addition, the B and H fields are assumed to be independent of radius. The period of the rotor PM is also independent of the radius and the wave number, k, is evaluated at the mean radius

$$k = \frac{P}{R_m} = \frac{2P}{R_o + R_i}. \tag{93}$$

Given these approximations, the vector potential due to the rotor PM, using (38), is

$$\hat{A}_{xn(m)} = \frac{4}{n\pi}\frac{B_r}{nk}\sin\left(\frac{n\pi}{2}\right) = \frac{2B_r}{n^2\pi}\frac{(R_o+R_i)}{P}\sin\left(\frac{n\pi}{2}\right). \tag{94}$$

$A^{(1)}_{xn(m)}$ simplifies to

$$\begin{aligned}\hat{A}^{(1)}_{xn(m)} &= -j\frac{\gamma_{\rm an}}{\mu_a}\left[\frac{\beta_{4n}-\beta_{2n}}{\alpha_{8n}\beta_{4n}-\alpha_{6n}\beta_{2n}}\right] \\ &\quad\times\sinh(\gamma_{\rm an}T_{\rm al})\,\hat{A}_{xn(m)} \\ &= -j\left(\frac{T_{\rm al}}{T_{\rm al}+T_{\rm cl}+T_{\rm ag}}\right)\hat{A}_{xn(m)}.\end{aligned} \tag{95}$$

The vector potential evaluated at half the thickness of the stator winding layer now becomes

$$\begin{aligned}\hat{A}_{xn,{\rm coil}(m)} &= \hat{A}^{(1)}_{xn(m)} \\ &= -j\frac{(R_o+R_i)}{P}\left(\frac{T_{\rm al}}{T_{\rm al}+T_{\rm cl}+T_{\rm ag}}B_r\right) \\ &\quad\times\frac{2}{n^2\pi}\sin\left(\frac{n\pi}{2}\right).\end{aligned} \tag{96}$$

To simplify things further, the spatial offset in the multiple turns of an N-turn/pole stator is ignored, and so the incremental flux/phase reduces to

$$\begin{aligned}\hat{\Phi}_{zn,{\rm coil}(m)} &= 2PN\hat{A}_{xn,{\rm coil}(m)}e^{j(n\pi/2)} \\ &= (R_o+R_i)\left(\frac{T_{\rm al}}{T_{\rm al}+T_{\rm cl}+T_{\rm ag}}B_r\right)N\frac{4}{n^2\pi}.\end{aligned} \tag{97}$$

Since (97) is independent of the radius, the flux linked by a phase becomes

$$\begin{aligned}\hat{\lambda}_{n,{\rm coil}(m)} &= (R_o-R_i)\,\hat{\Phi}_{zn,{\rm coil}(m)} \\ &= \left(R_o^2-R_i^2\right)\left(\frac{T_{\rm al}}{T_{\rm al}+T_{\rm cl}+T_{\rm ag}}B_r\right)N\frac{4}{n^2\pi}\end{aligned} \tag{98}$$

while the harmonic amplitudes of the open-circuit voltage are

$$\begin{aligned}\hat{V}_{\rm ocn} &= jn\omega_m\hat{\lambda}_{n,{\rm coil}(m)} \\ &= j\left(R_o^2-R_i^2\right)\left(\frac{T_{\rm al}}{T_{\rm al}+T_{\rm cl}+T_{\rm ag}}B_r\right)NP\Omega_m\frac{4}{n\pi}.\end{aligned} \tag{99}$$

The voltage harmonics can be added to generate the total open-circuit voltage

$$\begin{aligned}V_{\rm oc}(t) &= {\rm Re}\left\{\sum_{n=1,{\rm odd}}^{\infty}\hat{V}_{n,{\rm coil}(m)}e^{jn\omega_m t}\right\} \\ &= V_o\sum_{n=1,{\rm odd}}^{\infty}-\frac{4}{n\pi}\sin(\omega_m t)\end{aligned} \tag{100}$$

where

$$V_o = \left(R_o^2-R_i^2\right)\left(\frac{T_{\rm al}}{T_{\rm al}+T_{\rm cl}+T_{\rm ag}}B_r\right)NP\Omega_m. \tag{101}$$

The term inside the summation of (100) is the Fourier components of a square wave. Therefore, the open-circuit voltage due to a square-wave magnetization is also a square wave with magnitude V_o. The first term in parentheses in (101) shows how the open-circuit voltage scales with the active area of the machine. The second term in parentheses is the B field in the air gap and shows that the thickness of the rotor PM should be larger than the thickness of the coil layer and physical air gap combined in order to maximize the flux generated from the rotor PM. Last, the open-circuit voltage scales linearly with B_r, N, P, and Ω_m.

B. Stator Inductance

The stator inductance can be determined in the same manner as the open-circuit voltage. The total flux generated by the stator currents and linked by a single phase of the machine is found by integrating the incremental flux at a given radius over the radial span of the machine. The incremental flux linked by a single phase is P times the flux/pole. Referring back to Fig. 7, the incremental flux/phase in phase A of a 1-turn/pole machine is

$$\begin{aligned}\hat{\Phi}_{zn,{\rm coil}(j)} &= P\hat{A}_{xn,{\rm coil}(J)}\left(e^{-jnk(-(\lambda/4))}-e^{-jnk(\lambda/4)}\right) \\ &= 2P\hat{A}_{xn,{\rm coil}(J)}e^{j(n\pi/2)}\end{aligned} \tag{102}$$

where $\hat{A}_{xn,{\rm coil}(J)}$ is the vector potential due to the stator currents evaluated at half the thickness of the stator winding layer

$$\hat{A}_{xn,{\rm coil}(J)} = \left(\alpha_{1n}\hat{A}^{(1)}_{xn(J)}+\beta_{5n}\hat{A}^{(6)}_{xn(J)}\right)\frac{\sinh(0.5\gamma_{0n}T_{\rm cl})}{\sinh(\gamma_{0n}T_{\rm cl})}. \tag{103}$$

For the general case of a three-phase surface-wound machine with P pole pairs, N-turns/pole, κ winding layers, and $N' = N/\kappa$, the incremental flux/phase is

$$\hat{\Phi}_{zn,{\rm coil}(J)} = 2\kappa P\hat{A}_{xn,{\rm coil}(J)}\sum_{\substack{\nu=2N'+1\\ \text{step } 2}}^{4N'-1}e^{j(n\pi/6N')\nu}. \tag{104}$$

The stator currents, which have a single temporal frequency (ω_e), generate magnetic fields with multiple spatial harmonics. However, due to the large air gap, the higher order harmonic components are much smaller than the fundamental. Therefore, the flux linked by a winding due to the stator currents is composed of essentially the fundamental component of magnetic field in the air gap. Integrating over the radial span of the machine, the flux linked by a single phase is

$$\hat{\lambda}_{{\rm coil}(J)} = \int_{r=R_i}^{r=R_o}\hat{\Phi}_{z1,{\rm coil}(J)}dr. \tag{105}$$

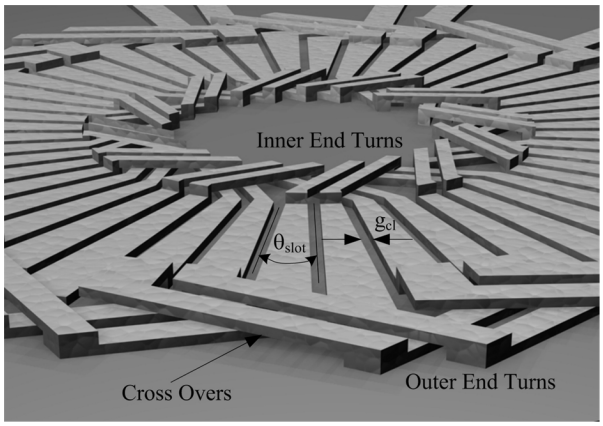

Fig. 19. Winding pattern for a 2-turn/pole, 8-pole machine. The radial conductors are unlaminated and connected by cross overs.

Note that this is the flux linkage generated by the sum of the three phase currents. The resulting inductance L_d is known as the synchronous inductance [14] and is given by

$$L_d = \frac{\mathrm{Re}\left\{\hat{\lambda}_{\mathrm{coil}(J)}\right\}}{I_o}. \tag{106}$$

Phase B and C currents produce a flux linked by phase A that is proportional to the $\cos(\pm(2/3)\pi) = -(1/2)$. Since $i_b + i_c = -i_a$, the sum of the fluxes produced by phase B and C equals half the flux produced by phase A. Phase A will see 1.5 times the flux produced by currents in only phase A. Therefore, the stator phase inductance L_s in the single-phase model will be

$$L_s = \frac{2}{3I_o}\mathrm{Re}\left\{\hat{\lambda}_{\mathrm{coil}(J)}\right\}. \tag{107}$$

C. Stator Resistance

For a surface-wound machine, the radial conductors of all three phases will occupy the same winding layer. The radial conductors in the same phase are connected by end turns that cross over end turns of the other phases as depicted in Fig. 19. The surface-wound stators in [13] all use full-pitched windings.

The radial conductor in each slot can be unlaminated as shown in Fig. 20(a) or laminated as shown in Fig. 20(b). Laminated radial conductors can be used to reduce proximity eddy current losses. There are $2PN$ radial conductors per phase so that the maximum angular span or slot angle for each conductor is

$$\theta_{\mathrm{slot}} = \frac{2\pi}{6PN} = \frac{\pi}{3PN}. \tag{108}$$

If there are C_{lam} laminations per radial conductor than the width of the laminated conductors is given by

$$W_{\mathrm{cl}}(r) = \frac{\pi r}{3PNC_{\mathrm{lam}}} - g_{\mathrm{cl}} \tag{109}$$

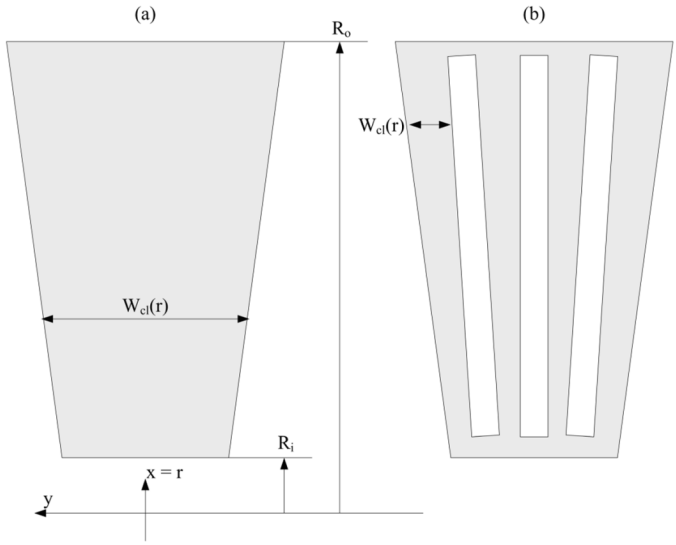

Fig. 20. Radial Conductors in a single slot: (a) unlaminated and (b) laminated.

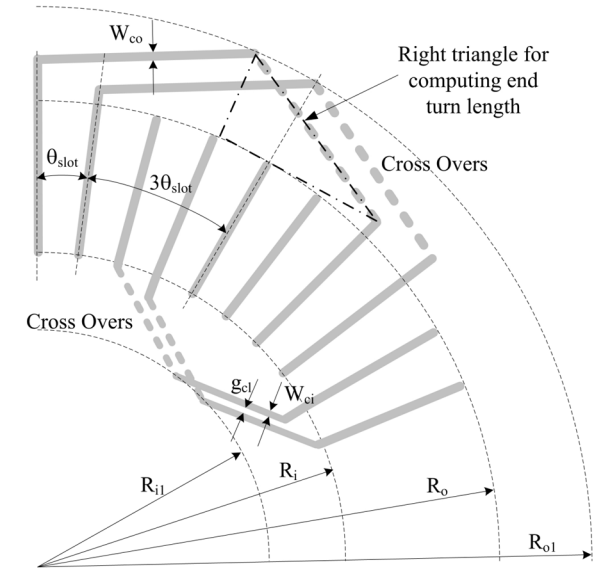

Fig. 21. End turn connections for a 2-turn/pole full-pitched winding.

where g_{cl} is the minimum distance between adjacent conductors imposed by fabrication constraints. The resistance of a radial conductor is

$$\begin{aligned} R_{\mathrm{conductor}} &= \frac{1}{\sigma_c T_{\mathrm{cl}}}\int_{R_i}^{R_o}\frac{dr}{W_{\mathrm{cl}}(r)} \\ &= \frac{3PNC_{\mathrm{lam}}}{\pi\sigma_c T_{\mathrm{cl}}}\ln\left(\frac{W_{\mathrm{cl}}(R_o)}{W_{\mathrm{cl}}(R_i)}\right) \end{aligned} \tag{110}$$

where T_{cl} is the height of the radial conductor and σ_c is the conductivity of copper. Consequently, the resistance of all the radial conductors in a single phase is

$$R_{\mathrm{radial}} = \frac{6\left(PNC_{\mathrm{lam}}\right)^2}{\pi\sigma_c T_{\mathrm{cl}}}\ln\left(\frac{W_{\mathrm{cl}}(R_o)}{W_{\mathrm{cl}}(R_i)}\right). \tag{111}$$

For full-pitched windings, like the one shown in Fig. 21, the length of all the end turns are the same. The end turns are made of straight conductors that each span $1.5N\theta_{\mathrm{slot}}$ radians ($3\theta_{\mathrm{slot}}$

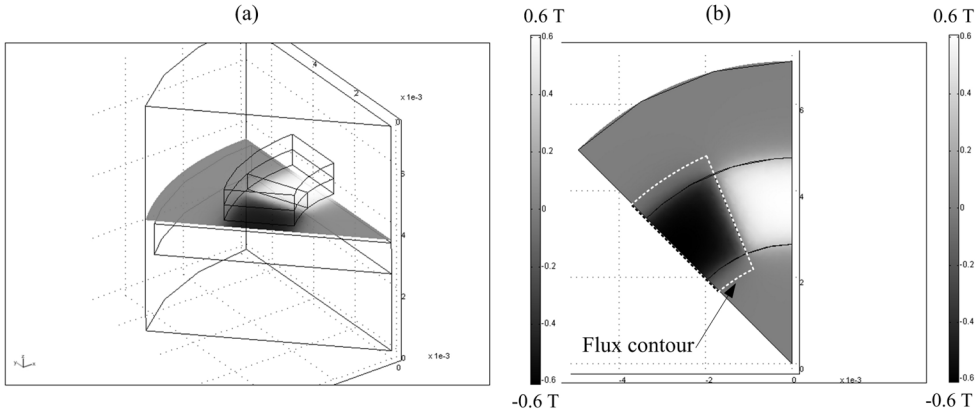

Fig. 22. Eight-pole axial magnetic flux density 100 μm above the surface of a planar PM machine stator: (a) perspective view and (b) top view.

radians for the 2-turn/pole machine as shown in Fig. 21). The length of the outer end turn conductors can be approximated as the hypotenuse of a right triangle

$$L_{\text{outer}} = \sqrt{\left(\frac{3}{2}N\theta_{\text{slot}}R_o\right)^2 + (R_{o1} - R_o)^2} = \sqrt{\left(\frac{\pi R_o}{2P}\right)^2 + (R_{o1} - R_o)^2}. \quad (112)$$

Since there are two conductors per end turn and NP end turns per phase, the resistance of the outer end turns is

$$R_{\text{outer}} = \frac{2NPL_{\text{outer}}}{\sigma_c T_{co} W_{co}} \quad (113)$$

where T_{co} and W_{co} are the height and width of the outer end turns, respectively.

The inner end turns are handled in a similar manner. The length of the inner end turn conductors is

$$L_{\text{inner}} = \sqrt{\left(\frac{\pi R_i}{2P}\right)^2 + (R_i - R_{i1})^2}. \quad (114)$$

The corresponding resistance of the inner end turn is

$$R_{\text{inner}} = \frac{2NPL_{\text{inner}}}{\sigma_c T_{ci} W_{ci}} \quad (115)$$

where T_{ci} and W_{ci} are the height and width of the outer end turns, respectively. The total resistance per phase is $R_{\text{radial}} + R_{\text{inner}} + R_{\text{outer}}$.

V. Results

A. FEA Analysis

To verify that the analytical model can accurately predict open-circuit voltages, 3-D FEA simulations of a prototype PM machine are done using FEMLAB (version 3.1). The rotor consists of an annular PM and back iron with an outer diameter of 9.525 mm and an inner diameter of 5.525 mm, and each with a thickness of 500 μm. The rotor is suspended 300 μm above the stator core, which is modeled as a large disk that extends well beyond the outer radius of the rotor. This is done because initial PM machines will be fabricated on ferromagnetic wafers. The 300-μm gap between the rotor and stator emulates the 100-μm physical air gap and 200-μm-thick surface windings.

In the model, the rotor–stator assembly is surrounded by air, and periodic boundary conditions are imposed. Due to the symmetry of the system, only $1/2P$ of the assembly was modeled, as shown in Fig. 22(a). Hiperco 50 is used as the rotor back iron material and Moly Permalloy is used as the stator core material. The annular PM has an ideal square wave magnetization profile with B_r set to 1 T and a permeability of μ_0 to simulate an SmCo magnet.

Using the nonlinear B–H curves for both the Moly Permalloy and Hiperco 50, a 3-D magneto-static FEA model is used as input into a nonlinear solver, and the magnetic fields in the machine for a stationary rotor are calculated. The resulting axial (z-direction) B-field distribution 100 μm above the stator core (half the height of the stator windings) is then extracted, as shown in Fig. 22(b) for an 8-pole machine. The z-directed B field is then input into a MATLAB script. The script solves for the voltage induced on a winding of arbitrary shape by solving for the time-derivative of the flux through a predefined contour as the magnetic field pattern is rotated at the synchronous speed.

The contour over which the B field is integrated is varied in order to simulate various winding patterns. For instance, the winding can have the same radial span as the rotor PM or it can extend beyond the inner and outer radii of the PM by some distance in order to capture the leakage flux, and thus maximize the voltage. Fig. 23 shows the variation in the open-circuit voltage as a function of the radial extension beyond the PM annulus. A contour that is concentric with the PM (i.e., same radial span) encloses 86% of the voltage that can be obtained if all the leakage flux is linked. Therefore, there is very little radial fringing in the magnetic fields even with an air gap as large as 300 μm. For a winding extending only 0.25 mm beyond both the inner and outer radii, 96.7% of the maximum voltage is captured, whereas a winding extending of 1 mm is assumed to capture all of the leakage flux. Thus, the 1-mm extension is used for comparison to the 2-D analytical model, because the 2-D model does not capture radial fringing flux.

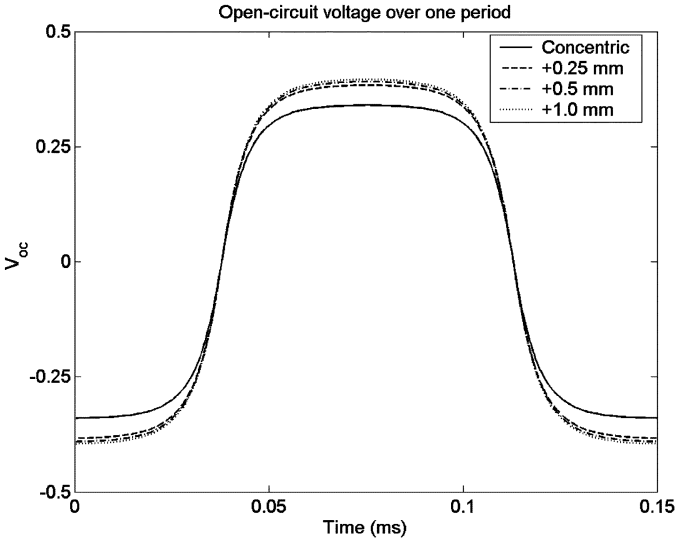

Fig. 23. Open-circuit voltage for different radial spans of the contour of integration of the magnetic flux.

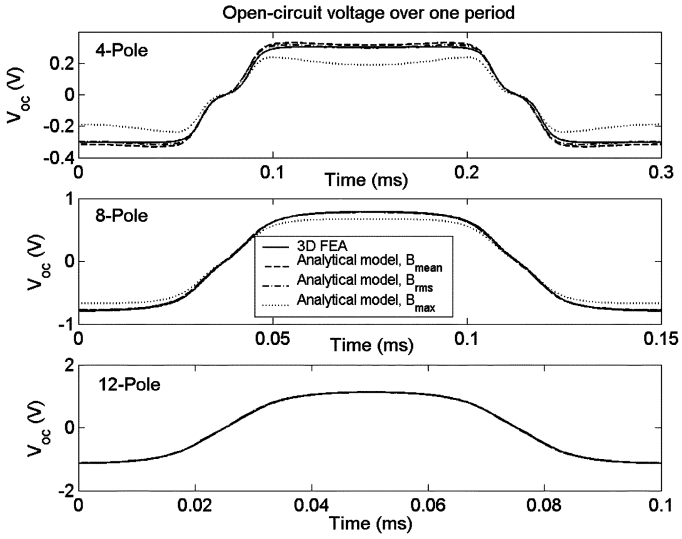

Fig. 24. Open-circuit voltage over one period for the 4-, 8-, and 16-pole machines. Dotted lines represent FEA; solid lines represent analytical model.

B. Model Validation

As discussed in the companion paper [13], the stator core is not an annulus concentric with the rotor, but, instead of a large wafer, the flux from the rotor PM will have more area to flow horizontally through the stator. This will lead to a smaller flux density in the stator than if it were only an annulus of ferromagnetic material. From the 3-D FEA analysis, a stator winding that has a radial span 1.25 times that of the rotor captures 96.7% of the maximum voltage possible. Therefore, the "effective" radial span of the stator will be 1.25 times the radial span of the rotor so that the average B field in the stator is taken to be 80% of the value calculated by (66).

Fig. 24 shows a comparison of open-circuit voltage waveforms predicted by the analytical model to the FEA results for machines with different number of poles, all with 2-turns/pole and with the rotor spinning at 100 krpm. Notice that for a 4-pole machine, using $B_{\rm mean}$ to determine the relative permeabilities of the rotor and stator core leads to and over prediction of the open-circuit voltage, while using $B_{\rm max}$ under predicts the open-circuit voltage. Using $B_{\rm rms}$ also over predicts the open-circuit voltage but the error is much smaller. For an 8-pole machine, the rotor and stator cores are less saturated and the open-circuit voltage predicted by using $B_{\rm mean}$ and $B_{\rm rms}$ converge to the same answer while the open circuit voltage predicted by using $B_{\rm max}$ is still smaller then the FEA result. With a 16-pole machine, the B fields in the rotor and stator cores are far from the saturation limit an all three B field values converge to the same open-circuit voltage. This makes sense since $B_{\rm mean}$ will give an optimistic value for the relative permeability while $B_{\rm max}$ will give a conservative estimate. Since $B_{\rm rms}$ is always larger then $B_{\rm mean}$ but less then $B_{\rm max}$, using the rms of the B field will predict an open-circuit voltage in between the value predicted be using the other two metrics and so is likely the best choice in all cases.

The rms voltage as a function of pole count is shown in Fig. 25. For a 2-pole machine, the errors in open-circuit voltages between the FEA and analytical results using $B_{\rm mean}$, $B_{\rm rms}$, and $B_{\rm max}$ are 18%, 7%, and -37%, respectively. For a

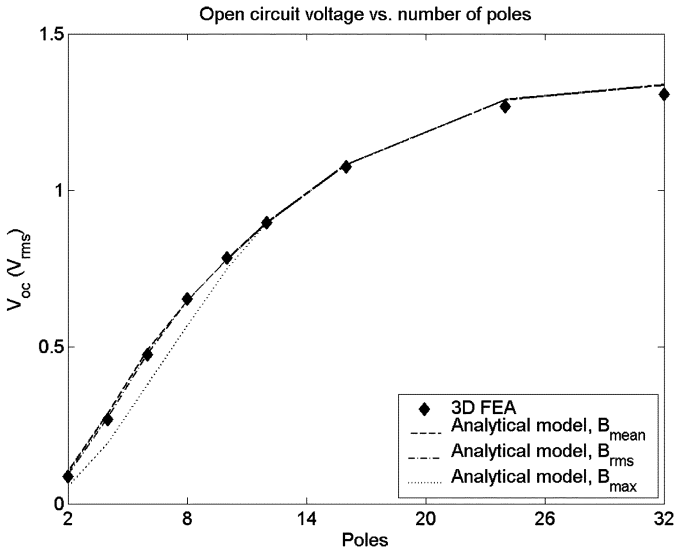

Fig. 25. Open-circuit voltages versus number of poles.

4-pole machine, the errors are 7%, 2.5%, and -28%, while an 8-pole machine the errors are 1%, 1%, and -13%. For higher pole counts, using any of the B field values matches the FEA result. From Fig. 25, it can be seen the using $B_{\rm rms}$ to compute the effective permeabilities for the rotor and stator core give the most accurate result over the widest range of machine poles.

Notice that, for a small number of poles (2–8), the increase in voltage is somewhat linear, while for larger pole counts $(12+)$, there are diminishing returns. To understand why the voltage does not increase linearly with pole number in Fig. 25, recall that the magnetic fields in the air gap decay away from the rotor PM with an exponential rate proportional to P, which is the number of pole pairs. For small P, the decay rate is small, and therefore the magnetic fields produced by the rotor PM are not significantly diminished as they reach the stator surface. For large values of P, the decay rate is large enough that magnetic fields at the stator surface are greatly reduced. From a physical standpoint, as the number of poles increases, the width of each pole

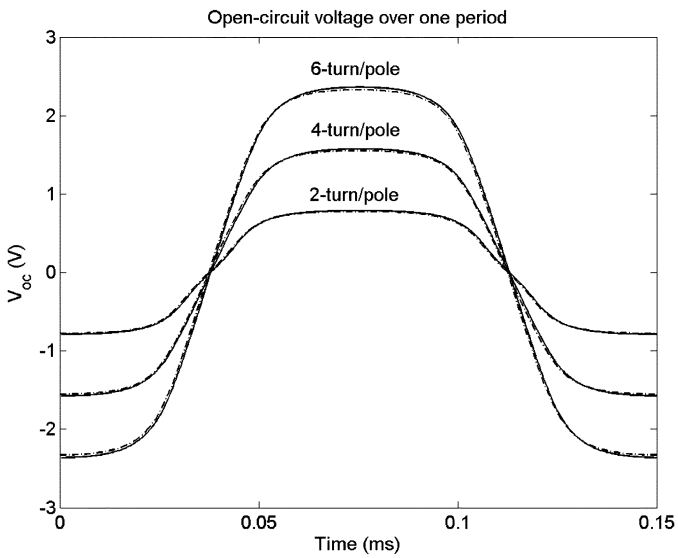

Fig. 26. Open-circuit voltage over one period for 2-, 4-, and 6-turn/pole machines. Dotted lines represent FEA; solid lines represent analytical model.

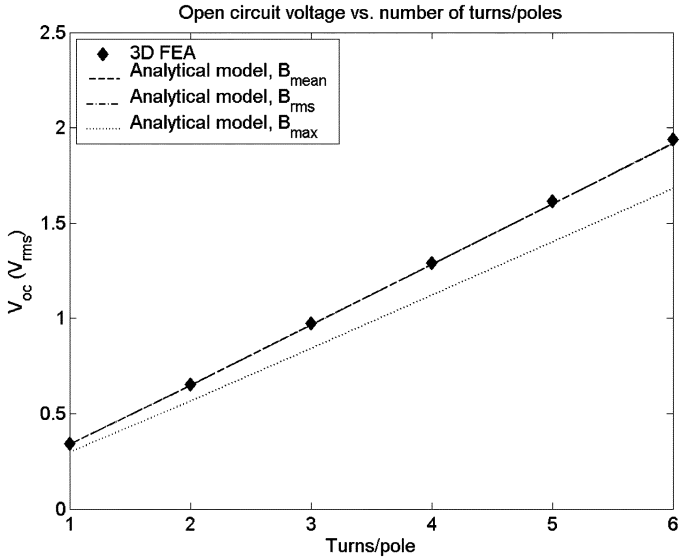

Fig. 27. Open-circuit voltage versus number to turns/pole.

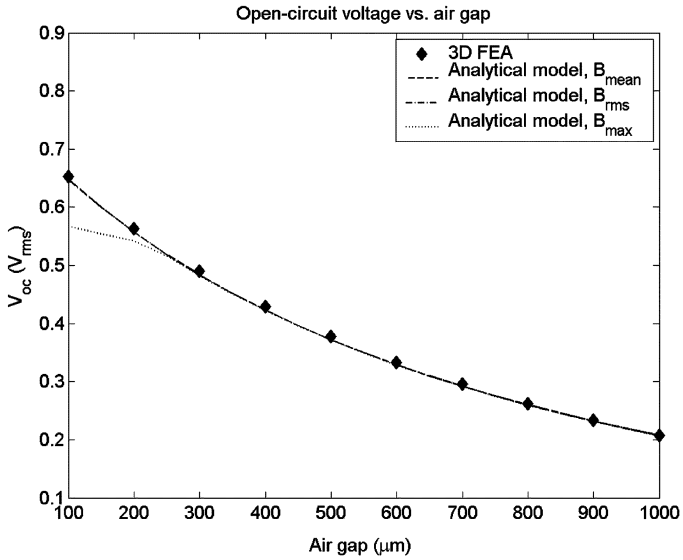

Fig. 28. Open-circuit voltage versus air gap.

decreases since the circumference of the PM annulus is constant. When the poles become tightly packed the flux lines between adjacent north and south poles are short enough that they connect to each other without passing through the stator core. Thus, the flux linked by the stator windings decreases.

Fig. 26 shows open-circuit voltage waveforms for an 8-pole machine at 100 krpm with 2-, 4-, and 6-turn/pole stators. The analytical model uses $B_{\rm rms}$ resulting in a good match between the FEA and analytical results. Fig. 27 shows the rms voltage versus turn/pole. The open-circuit voltages obtained by using $B_{\rm rms}$ and $B_{\rm rms}$ produce the same results, so the two curves lie on top of one another. Notice that the continuum model shows a relatively linear slope which means that the spatial offset in adjacent turns of a multiple turn/pole machine have a small effect on the open-circuit voltage.

Fig. 28 shows open-circuit voltage as a function of air gap for an 8-pole, 2-turn/pole machine at 100 krpm. The voltage decreases exponentially with air gap, as expected. Using $B_{\rm max}$ underpredicts the open-circuit voltage at an air gap of 100 μm. As the air gap increases, the flux density in the rotor and stator cores decrease and the cores become unsaturated. This leads to a convergence of the analytical model using three B field values. The analytical predictions agree extremely well with the FEA results.

Note that the FEMLAB simulations solve a static problem. The resulting magnetic field solutions do not incorporate the effects of eddy currents in the stator that would be present due to a spinning PM rotor. In the analytical model, there is only a small discrepancy between the open-circuit voltages predicted from machines with conducting and nonconducting stators (Fig. 29). The eddy currents generated in the conductive stator due to the spinning PM create their own magnetic fields that try to prevent the PM flux from coupling to the stator. However, due to the large air gap, the magnetic fields generated are very small and have negligible effects on the open-circuit voltage.

Using $B_{\rm rms}$ to compute the relative permeabilities in the rotor and stator cores and setting $\sigma_s = 1.6 \times 10^6$ S for a Moly Permalloy stator, an 8-pole machine has a 4.7% difference in the open-circuit voltages between conductive and nonconductive stators. As the number of poles decreases, the two curves converge because the stator core begins to saturate and the induced eddy currents become smaller. At higher pole counts, the permeability of the stator core is so high that the reduced reluctance in the stator core due to the presence of eddy currents produces a negligible effect on the open-circuit voltage.

The discrepancy between the open-circuit voltage of conductive and nonconductive stators also decreases with air gap (Fig. 29). The eddy currents increase the flux density in the stator core by constraining the flux to flow with the penetration depth γ_{sn}. This results in a lower permeability for the stator and therefore a lower rms voltage. As the air gap increases, the reluctance of the air gap increases which reduces the impact of the lower permeability in the stator and makes the rms voltages for the conducting and nonconducting converge.

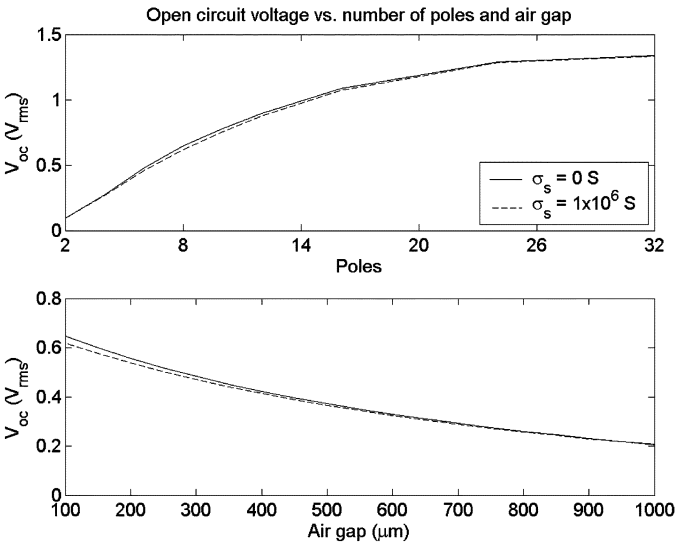

Fig. 29. Open-circuit voltage versus poles and air gap for conductive and nonconductive stators.

VI. Conclusion

The modeling of planar axial-flux surface-wound PM machines is presented. The machines are modeled as a set of continuum planar layers. The 3-D field solutions for the machine are constructed by integrating 2-D Cartesian coordinated solutions over the radial span of the machine. The effects of saturation in the rotor and stator cores are incorporated into the model through the use of effective permeabilities. Hysteresis loss is computed using the BH curve of the core material, while eddy current losses in the stator core are computed using the Maxwell Stress Tensor. It was found that using the rms values for the B fields in the rotor and stator core to compute relative permeabilities provided the most accurate results over the widest range of machine dimensions and thus should be used in most cases. Proximity eddy currents in the stator windings due to the magnetic fields from the rotor magnet are also computed. The proximity loss is modeled separately using the field solutions from the continuum model as inputs.

From the field solutions, an equivalent per-phase circuit model is then derived and consists of an open-circuit voltage, stator inductance, and stator resistance. The continuum model for the surface wound PM machine is compared to FEA analysis and agrees extremely well with the numerical results over a wide variation in the number of poles, turns/pole and air gap (under the assumption that all of the radial leakage flux is linked by the stator windings). Extensive experimental verification of the model is described in [13].

The models presented here are computationally fast. For example, it takes only a few minutes of computation time to generate plots of output voltage as a function of various dimensional design parameters (e.g., Figs. 25, 27, and 28). Comparatively, to generate a few similar data points using 3-D FEA requires hours of computational time. Thus, these models enable the rapid performance modeling of a variety of design configurations. This is especially important when considering the integration of the generator within a more complicated microengine power generation system, where many system-level tradeoffs may need to be explored.

References

[1] S. A. Jacobson and A. H. Epstein, "An informal survey of power MEMS," in *Proc. Int. Symp. Micro-Mechanical Engineering,*, Tsuchiura and Tsukuba, Japan, Dec. 1–3, 2003, pp. 513–520.

[2] A. H. Epstein, "Power MEMS and microengines," in *Dig. Tech. Papers Transducers '97 Conf.*, Chicago, IL, Jun. 16–19, 1997, pp. 753–756.

[3] F. Cros, H. Koser, M. G. Allen, and J. H. Lang, "Magnetic induction micromachine—Part II: Fabrication and testing," *J. Microelectromech. Syst.*, vol. 15, no. 2, pp. 427–439, Apr. 2006.

[4] D. P. Arnold, S. Das, F. Cros, I. Zana, J. H. Lang, and M. G. Allen, "Magnetic induction machines integrated into bulk-micromachined silicon," *J. Microelectromech. Syst.*, vol. 15, no. 2, pp. 406–414, Apr. 2006.

[5] O. Cugat, J. Delamare, and G. Reyne, "Magnetic micro-actuators and systems (MAGMAS)," *IEEE Trans. Magn.*, vol. 39, no. 6, pp. 3607–3612, Nov. 2003.

[6] B. Wagner, M. Kreutzer, and W. Benecke, "Permanent magnet micromotors on silicon substrates," *J. Microelectromech. Syst.*, vol. 2, no. 1, pp. 23–29, Feb. 1993.

[7] P.-A. Gilles, J. Delamare, O. Cugat, and J.-L. Schanen, "Design of a permanent magnet planar synchronous micromotor," in *Proc. 35th Mtg. IEEE Industry Appl. Soc.*, Oct. 2000, vol. 1, pp. 223–227.

[8] C. Yang, "An axial flux electromagnetic micromotor," *J. Micromech. Microeng.*, vol. 11, pp. 113–117, 2001.

[9] H. Raisigel, O. Cugat, J. Delamare, O. Wiss, and H. Rostaing, "Magnetic planar micro-generator," in *Proc. Transducers'05: 13th Int. Conf. Solid-State Sensors, Actuators and Microsystems*, Seoul, Korea, pp. 757–761.

[10] A. S. Holmes, G. Hong, and K. R. Buffard, "Axial-flux permanent magnet machines for micropower generation," *J. Microelectromech. Syst.*, vol. 14, no. 1, pp. 54–62, Feb. 2005.

[11] J. L. Kirtley, Jr and H. W. Beaty, *Electric Motor Handbook*. New York: McGraw-Hill, 1998.

[12] D. L. Trumper, W.-J. Kim, and M. E. Williams, "Design and analysis framework for linear permanent-magnet machines," *IEEE Trans. Ind. Appl.*, vol. 32, no. 2, pp. 371–379, Mar./Apr. 1996.

[13] D. P. Arnold, S. Das, J.-W. Park, I. Zana, J. H. Lang, and M. G. Allen, "Microfabricated high-speed axial-air-gap multiwatt permanent-magnet generators—Part II: Fabrication and testing," *J. Microelectromech. Syst.*, vol. 15, no. 5, pp. 1351–1363, Oct. 2006.

[14] A. E. Fitzgerald, C. Kingsley, Jr, and S. D. Umans, *Electric Machinery*, 6th Ed ed. New York: McGraw Hill, 2002.

[15] J. L. Kirtley, Jr and E. Lovelace, "Drag loss in retaining rings of permanent magnet motors," in *Proc. Int. Electric Machines and Drives Conf. Dig. Tech. Papers*, Madison, WI, Jun. 1–4, 2004, vol. 2, pp. 1068–1072.

[16] H. Koser, Development of Magnetic Induction Machines for Micro Turbo Machinery. Cambridge, MA, Massachusetts Institute of Technology, 2002, Ph.D..

[17] J. R. Melcher, *Continuum Electromechanics*. Cambridge, MA: MIT Press, 1981.

[18] H. H. Woodson and J. R. Melcher, *Electromechanical Dynamics*. New York: Wiley, 1968.

[19] J. G. Kassakian, M. F. Schlecht, and G. C. Verghese, *Principles of Power Electronics*. Reading, MA: Addison-Wesley, 1991.

Sauparna Das (M'03) received B.S. degrees in electrical engineering and mathematics, the M.Eng. degree in electrical engineering, and the Ph.D. degree in electrical engineering from the Massachusetts Institute of Technology (MIT), Cambridge, in 2002, 2002, and 2005, respectively. He carried out his Master's thesis at Analog Devices Inc. under a fellowship from the MIT Electrical Engineering and Computer Science Internship program designing high-frequency dc–dc converters for cell phone power applications (2001–2002). His doctoral thesis focused on the development of magnetic machines and power electronics for Power-MEMS applications.

He is currently a Design Engineer with Linear Technology, North Chelmsford, MA, designing power management ICs for portable electronic devices. His interests include the modeling, design, and control of electromechanical systems and power electronics.

Dr. Das is a member of Eta Kappa Nu.

David P. Arnold (S'97–M'04) received B.S. degrees in electrical engineering and computer engineering and the M.S. degree in electrical engineering from the University of Florida, Gainesville, in 1999, 1999, and 2001, respectively, and the Ph.D. degree in electrical engineering from the Georgia Institute of Technology, Atlanta, in 2004.

In 2005, he joined the Department of Electrical and Computer Engineering, University of Florida, as an Assistant Professor. His research focuses on the design, fabrication, and characterization of magnetic and electromechanical microsensors/microactuators, as well as miniaturized power and energy systems.

Dr. Arnold is a member of Eta Kappa Nu, Tau Beta Pi, and the American Society for Engineering Education.

Iulica Zana (M'98) received the B.S. and M.S. degrees in materials science and engineering from the University "Politechnica" of Bucharest, Bucharest, Romania, in 1994 and 1995, respectively, and the Ph.D. degree in metallurgical and materials engineering from the University of Alabama, Tuscaloosa, in 2003.

From 2003 to 2004, he held a postdoctoral appointment with Prof. M. G. Allen's group at the Georgia Institute of Technology, Atlanta. He is currently a Postdoctoral Research Fellow with the Center for Materials for Information Technology, University of Alabama. He has been working on the development and implementation of high-performance magnetic materials into new microfabricated magnetic devices. His research interests span from deposition to characterization of magnetic materials.

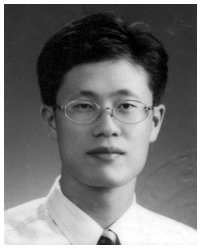

Jin-Woo Park received the B.S. degree in electrical engineering from Sung Kyun Kwan University, Seoul, Korea, in 1996, and the M.S. and Ph.D. degrees in electrical and computer engineering from the Georgia Institute of Technology (Georgia Tech), Atlanta, in 2000 and 2004, respectively.

After graduation, he was a Postdoctoral Fellow with Georgia Tech. Currently, he is with Cardiomems Inc, Atlanta, as a MEMS Project Engineer. His research interests include design and fabrication of wireless MEMS pressure sensors for biomedical applications and micromachined magnetic components for compact power applications.

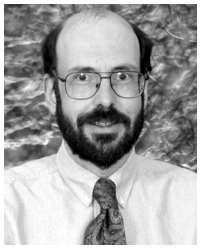

Mark G. Allen (M'89–SM'95) received the B.A. degree in chemistry, the B.S.E. degree in chemical engineering, and the B.S.E. degree in electrical engineering from the University of Pennsylvania, Philadelphia, in 1984, and the S.M. and Ph.D. degrees in microelectronic materials from the Massachusetts Institute of Technology, Cambridge, in 1986 and 1989, respectively.

He joined the faculty of the Georgia Institute of Technology, Atlanta, in 1989, where he currently holds the rank of Professor and the J. M. Pettit Professorship in Microelectronics. His research interests are in the areas of micromachining and microelectromechanical systems (MEMS), in particular the development and application of new fabrication technologies for micromachined devices and systems.

Prof. Allen was General Co-Chair of the 1996 IEEE MEMS conference and is the North American Editor of the *Journal of Micromechanics and Microengineering.*

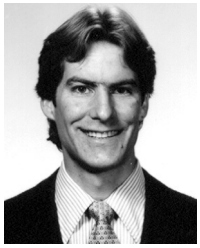

Jeffrey H. Lang (S'78–M'79–SM'95–F'98) received the S.B., S.M., and Ph.D. degrees from the Department of Electrical Engineering and Computer Science, Massachusetts Institute of Technology (MIT), Cambridge, in 1975, 1977, and 1980, respectively.

He joined the faculty of MIT in 1980, where he is now a Professor of Electrical Engineering and Computer Science. He served as the Associate Director of the MIT Laboratory for Electromagnetic and Electronic Systems between 1991 and 2003 and as an Associate Editor of *Sensors and Actuators* between 1991 and 1994. His research and teaching interests focus on the analysis, design, and control of electromechanical systems with an emphasis on rotating machinery, micro-scale sensors and actuators (MEMS), and flexible structures. He has written over 180 papers and holds 11 patents in the areas of electromechanics, power electronics, and applied control. He is also the coauthor of *Foundations of Analog and Digital Electronic Circuits* (Morgan Kaufman, 2005).

Prof. Lang is a former Hertz Foundation Fellow and has been awarded four best-paper prizes from IEEE societies.